Implementation of a Particle Image Velocimetry (PIV) system — An example application of PIV to wake — flows behind objects —

October, 1 9 9 6

Oarai Engineering Center

Power Reactor and Nuclear Fuel Development Corporation

Implementation of a Particle Image Velocimetry (PIV) system
– An example application of PIV to wake-flows behind objects –

A. Tokuhiro[1], K. Hishida[2] and Y. Ohki[3]

Abstract

Particle Image Velocimetry (PIV) describes a velocity measurement technique for gas and liquid flows whereby, as the name implies, movement of tracer particles in motion with the flow are recorded as images. The particles are frame-to-frame "tracked" by one of several correlation techniques from which a 2D vector field can be generated. A 3D vector field is also possible. The measurement method takes advantage of current computer, CCD camera and laser light technologies for its image processing needs. A laser light sheet is typically used to illuminate the tracer particles in the flow field of interest and when implemented accentuates the constrast between the particle and the transparent medium. One can also apply Laser Induced Fluorescence (LIF) in order to further distinguish the tracer particles, the transparent, continuous medium and any light reflecting surfaces in the flow field such as the interface of a gas bubble rising in a liquid. It is also possible to deduce the temperature field from LIF images.

In the present work an introduction to PIV is given by way of an example. The selected flow configuration is that of wake-flow behind a bubble and its solid equivalent. By solid equivalent we mean a solid model with approximately the equivalent bubble breadth and volume. This two-component, two-phase flow aptly demonstrates the applicability of PIV to spatio-temporal flows. Use was additionally made of an Infrared Shadow Technique (IST) in order to capture the unlit image (shadow) of the bubble or solid within the flow field. By triggering both the laser and infrared light sources with the CCD camera, the shape of the object as well as the flow field was simultaneously recorded. Besides the 2D vector field, calculations of the vorticity, Reynolds stress and turbulent kinetic energy (*tke*) distributions were made. The results indicate that for counter-current flow (U_{avg}~0.245 m/s) of water in a square channel (100 mm) with a single air bubble of roughly 10 mm diameter (Re_{Db} ~ 10^4) one could conclude the following: 1) PIV can detect differences in the wake flow field behind a bubble and that behind an equivalently sized solid. The difference of course stems from the surface boundary condition (slip versus non-slip), 2) the wake flow field behind the bubble is spatio-temporal due to the oscillation of the bubble; that is, the velocity, vorticity and *tke* distributions change with the oscillatory motion, and 3) as the bubble tries to minimize the energy-loss associated with its inherent motion it does so by distributing the hydrodynamic *tke* uniformly in the wake-field whereas in the case of the solid, the energy is distributed in a confined region in the near-wake. The order of magnitude of the *tke* is however similar which strongly suggests leads us to believe that the energy dissipation mechanisms are different in the two cases.

I

We also made a limited comparison of velocity data obtained via DPIV and ultrasound Doppler velocimetry. Measurements were once again conducted using the Ultrasound Velocity Profile monitor (UVP) and validate our PIV results; that is, the magnitudes and trends of the velocity and velocity-derived data agree with the PIV produced results.

---

1 Reactor Engineering Section, Safety Engineering Division, PNC International Fellow.
2 Reactor Engineering Section, Safety Engineering Division, Guest Scientist from Keio University, Mechanical Engineering Department.
3 Reactor Engineering Section, Safety Engineering Division.

粒子画像流速測定（PIV）の実施
物体後流における PIV の適用事例

A. Tokuhiro[1] , K. Hishida[2] and Y. Ohki[3]

要旨

粒子画像流速測定法(PIV)は、流れの中のトレーサー粒子の挙動を画像として記録することにより、流体の流れを測定する技術である。粒子は各フレーム毎に痕跡が記録され、相互相関により、２次元の流速場を得ることが出来る。これにより、３次元の流速場の測定も可能である。この測定法の画像処理にはコンピュータ、CCD カメラ、レーザー光が必要である。レーザーシートは流速場を得るべき面の粒子を発光させるために使用され、粒子と周辺流体とのコントラストを顕著にする。また、トレーサー粒子と流体や流体中を上昇する気泡界面などのレーザー光の反射面をより区別する手法としてレーザー誘起蛍光法(LIF)の適用も考えられる。LIF による温度場の測定も可能である。

本書では、PIV の導入方法について適用事例を通して述べる。適用事例としては、気泡とそれと同等な固体の後流についての試験を行った結果を示す。気泡モデルとして、幅と体積が気泡と同等である固体モデルにより近似できるものとした。この２成分２相流により空間的、時間的に変化する流れに対してのPIVの適用を実証することが出来る。さらに流れ場中の気泡や固体の画像を得るために、赤外線投影法を使用した。レーザーと赤外線の画像を CCD カメラで同時に撮影することにより、流れ場と物体の影を同時に記録できた。２次元流速場と共に、渦度、レイノルズ応力、乱流運動エネルギー(tke)分布を算出した。水による、正方流路内(100mm)対向流(U_{avg}~0.246m/sec)中に約 10mm 径の空気泡を入れた試験を行い、次の結果を得た。

１）PIV は、気泡とそれと等価な大きさの固体の後方での後流について流れの違いを確認することが出来た。違いは気泡と固体の表面境界条件の違いにより生じるものである。
２）気泡後方の後流場は、気泡の振動により空間的、時間的に変化する。すなわち、流速、渦度、乱流運動エネルギー分布は、振動挙動を伴った変化をする。
３）気泡は、自分自身の運動によるエネルギー損失を最小にするように振る舞うため、乱流運動エネルギーを後流域に一様に分配するが、固体の場合では、乱流運動エネルギーは固体のごく近傍の制限された領域に分配される。しか

しながら、乱流運動エネルギーの値はほぼ同じオーダーであることから、2つのケースでは乱流運動エネルギー散逸のメカニズムが異なっていると推測できる。

また、PIVと超音波流速測定法により得られた一部の流速データに関して比較を行った。その結果、UVPによる流速や流速場から導かれたデータのオーダー、および傾向はPIVによる結果と一致した。

1　大洗工学センター、安全工学部、原子炉工学室、国際特別研究員
2　大洗工学センター、安全工学部、原子炉工学室、客員研究員、
　　慶応大学助教授
3　大洗工学センター、安全工学部、原子炉工学室

Contents

List of Figures

List of Figures in Appendices

List of Tables in Appendices

1. Introduction

In order to investigate thermal-hydraulic phenomena of relevance to LMFBR safety we conduct experiments using scaled facilities, separate-effects facilities and basic small-to-medium scale experiments. Regardless of the size of the experiment however, we require instrumentation in order to measure physical quantities such as temperature and pressure. Of particular importance in thermal-hydraulic experiments are temperature and velocity measurements since we wish to evaluate the convective heat transfer process. While there are a number of methods for temperature and velocity measurement non-intrusive techniques when the option is available, are preferred (over intrusive techniques) in order not to disturb the flow-field of interest. Specifically with regard to velocimetry laser Doppler, ultrasound Doppler and Particle Image (or Tracking) velocimetry qualify as non-intrusive techniques. Ultrasound Doppler can also be intrusive depending on the application.

The ultrasound Doppler technique has proven to be a useful tool in thermal-hydraulics as shown by a number of works by Takeda [1-4] and recently by Tokuhiro [5]. The technique is easy to set-up, to use (requires no calibration) and has a relatively "capable" measurement range in terms of distance and maximum/minimum velocities [see Appendix C, Table C-2]. It also appears to be one of the few velocimetry methods available for use in LMFBRs. It is thus of importance not only to explore, develop and expand the role of ultrasound Doppler velocimetry (UDV) in LMFBR thermal-hydraulics, but to validate the method by independent means; that is, either by numerical simulation of a similar configuration or by a second measurement method. Any method though it may be useful should however, be compared with UDV. In our case we have chosen Particle Image Velocimetry (PIV) as our second measurement method. The principle and details of PIV are discussed below.

The objective of our implementation of PIV as a measurement tool is mainly the validation of velocity data taken by UDV; that is, by the Ultrasound Velocity Profile (UVP) monitor. By using both PIV and UDV, the latter with the Model X-3, multiplexer and a number of transducers, we have two independent means to measure the same field of interest.

1.1 A Brief Introduction to PIV

Particle Image Velocimetry (PIV) is a velocity measurement technique applied to transparent fluids (gases and liquids) which has become prominent due to the availability of three modern devices, these being: 1) the video camera, 2) image processing boards such as the frame grabber and 3) modern (desktop) computers with sufficient processing speed, memory and digital signal processing (DSP) capability. In the years prior to the advent of these devices, related but more visualization-oriented techniques existed in form, for example in photographs and movies of streaklines, pathlines and streamlines of a flow field of interest. These concepts are described in standard textbooks on fluid dynamics, for example Fox and MacDonald [6]. Thus PIV can trace its concept to these precursors and still retains the simple ideas as follows. If one seeds a flow with tracer particles and with an image recording device (camera, movie camera, video camera etc.) records two successive images separated by a

relatively short but measured time span one can in principle track the movement of particles from one image to the next. By track we mean noting the displacement of each particle in the "original window" to the subsequent "interrogation window" with the additional assurance that the original particle is "most likely" the chosen particle in the interrogation window. Once this is established, by noting the time-span between images, the velocity vectors can be calculated. While the number of particles is relatively small, "particle tracking" is precise in its approach. However, many flow applications involve many particles, primarily for acceptable resolution of the phenomena, and consequently great demands are made on the computational means. This makes particle tracking unrealistic in terms of an "on-line" measurement method. On the other hand pulsed laser photography of many particles undergoing short displacements such as with Laser Speckle Velocimetry (LSV) and PIV do not require tracking. Nevertheless reliance on opto-mechanical techniques are time-consuming especially when they involve photographic development. We thus move to digital PIV (DPIV) and the use of a cross-correlational technique, which together consolidate many of the advantages of the above-mentioned systems. Here we utilize the processing speed and practicalities of digital technology while simultaneously bypassing particle tracking by using a cross-correlational technique on the acquired images. The one drawback, however, is the relatively poor spatial resolution which comes from identifying the particles as spatial gray particle groups in a small area of pixel matrix dimensions. The application of this method to fluid engineering nevertheless appears to demonstrate its relevance as a measurement tool. We thus hope to apply it to the thermal striping problem; that is, the study of mixing between thermally-stratified jets.

2. PIV methodology

2.1 PIV system components

Figure 1 shows a typical set-up for PIV. Since the hardware and software are continuously evolving the set-up as shown is more a functional representation than pieces of actual hardware. In this sense the hardware components can be divided into three functional groups: 1) light source, 2) camera and video-recorder and 3) computer. It is not the intent of the author to review the wide range of hardware components in use in various PIV systems. The objective is to highlight the function of the mentioned devices.

The light source is most commonly a laser sheet projected into the region of interest. In the case shown an Argon-Ion laser's beam traverses through an AOM or acoustic optical modulator. Equally other types of lasers can be utilized as well as various optical components (lens, filters etc.) in order to illuminate the flow field. The AOM is synchronized with the vertical signal of the CCD camera in our application. The laser sheet has a width of 1-2 mm.

As for the cameras and video recorders, though they often work in unison, each serves a different function. The choice of camera is determined on the characteristic velocity of flow (or characteristice time and length-scale); that is, while low-speed flows (on the order of 1-10 [mm/s]) may be handled with normal speed and

digital cameras, high-speed flows (order of 1-10 [m/s]) may require higher framing rate CCD cameras (~ 120 fps) if not high-speed movie cameras (1000-3000 fps) accompanied by digitization of selected images. Since for PIV the only real requirement is a sequence of digitized images, any camera-like device producing an direct or indirect digitized image can be used. In the present case a Photocam CCD camera was used.

As for video-recorders the video-tape on which data is written can be viewed as a storage medium or device in much the same context as opti-mechanical media such as CD-ROMs, various magnetic tape-drives, hard-drives and a host of others too many to mention. The function of the video-recorder is thus as a reading/writing device onto a selected medium which must be routinely accessible and when stored, as an archived source of data. The video-tape and video-recorder in this respect has served many PIV users well and continues to be a inexpensive and accessible data medium.

With the ongoing improvements in electronic memory residing in the computers however, it is possible to bypass the recording of the images onto a videotape format (thereby them VCR). So a variation on the above-described system is one without the VCR units and the frame grabber board. The images are output in digitized format from the CCD camera directly into a computer's memory. In our case the number of recorded images with a Photocam CCD camera (taken at 120 fps) in our PC (32 MB RAM) is 60-70. With this development then, the videotape becomes a means of archiving (backing-up) data. It is worth noting that roughly 10 seconds of video data consumes 1 G(iga)B of electronic memory.

By whatever means the images are recorded and stored, it is very important in PIV to keep track of the individual images. One way to accomplish this task is by bar-coding in order to "tag" the image frames. Thus each frame has an unique bar-code number which in our case consisted of a 24 bit binary number where one bit was a 8 x 8 pixel square of black or white corresponding to "0" and "1" respectively. This number was incremented with the CCD camera's vertical signal while the laser sheet was synchronized with the even number of the bar-code and illuminated a single pulse per video frame. This thus takes one image for both the odd and even fields.

Lastly the computer hardware itself can be any one of the commercially available platforms; that is, IBM-compatible, Apple/MacIntosh based, NEC-98 based or other as long as it can accomodate a frame grabber (if used), a Digital Signal Processor (DSP) board and for convenience a Local Area Network (LAN) board. Or it may be a specialized device such as a stand-alone high-speed digital camera with compatible output or part of a larger data acquisition/monitoring system with video capability. The functional role here is for much of the arithmetic operations used for a particular correlational technique to be performed "online" with a DSP or equivalent board. Use is then made of a LAN board to transfer the data, typically to an Engineering Work Station (EWS) where the data processing is finish and the data is presented in an acceptable manner.

It is worth noting that one particular piece of hardware of relative importance in the system is the timing controller. The controller serves to trigger the components in unison; that is, the laser sheet and other light sources (if used) and the vertical signal of CCD cameras are triggered together so that the data acquisition process is optimized in terms of capturing the best possible particle images. The particular device used in the present experiment was homemade.

As easily assembled as these hardware components are, the judicious implementation of a software package for data acquisition and processing is at the heart of any PIV system. It goes without saying that the software instructs the hardware components to work in unison and in sequence so that meaningful results are produced. Since producing a two-dimensional vector plot is the objective of many present day PIV systems, the programming means by which this is accomplished similar amongst, otherwise varied systems. It is therefore not surprising that commercial packages are presently available whereas just a few years before, most PIV users were also PIV developers; that is, most PIV systems were accompanied by in-house customized software packages. At the core of these PIV systems is the routine to identify a particle from frame-to-frame. This is accomplished via a "correlation" expressing the relationship of data "bits" to one another. A particular correlation that expresses the relationship of *two* data sets (two separate images in PIV) taken at different times is the *cross-correlation*. This correlation method as applied to PIV will be briefly described below. For more detailed information on correlation methods we cite Bendat and Piersol [7].

2.2 Cross-correlational technique

The principle of the cross-correlation technique as applied to PIV is shown in Figure 2. Starting with an original (sub)image or *reference* matrix of particle points at time $t=t_0$ (can be part of a larger window) we scan the subsequent image at time t_0+dt which we call the *interrogation* window. The location of the matrix *corresponding* (the corresponding matrix) to the *reference* matrix in the interrogation window is approximately known apriori since the inherent assumption of PIV is that the images change only "slightly". The particles themselves are then identified by the maximum coefficient of the cross-correlation between the *reference* and the area in question in the *interrogation* window. The velocity vector is subsequently evaluated from the displacement and time interval between the reference and corresponding matrix. The initial size of the correlated area is left as variable since the optimum size is dictated by the density of tracer particles and local strain rate of the flow field. When for instance the density of particles is low, the reference matrix contains very little "information" and the number of erroneously evaluated vectors is relatively high since the maximum correlation coefficient can be hard to find. From experience it is known that the reference matrix should contain more than 3 to 4 particles. Returning to the issue of the constraint that only "slight" changes in the captured images are accomodated in PIV, in terms of the types of flows this generally means that high shear flows cannot be handled. In fact Yamamoto et al. [8] has shown that the number of erroneous vectors (those facing a direction contrary to the surrounding vectors) increases with an increase in strain rate so that flows with large vorticity and shear tend to produce a large number of erroneously calculated vectors.

As this may be however, one cannot avoid flows with both high and low shear regions. In fact even with "preferred" low shear flows it is not uncommon that the correlation value of "another" vector exceeds that of the "correct" vector. Thus a cross checking verification procedure is usually implemented. In the present case the vectors are calculated over the entire plane while storing in memory the second and third highest correlation values and its displacements. If a given vector is considerably different from an "average" vector calculated from its surrounding vectors, the most similar vector with the second or third highest correlation was selected. This procedure is then repeated a number or times; in fact, 5-6 times was judged sufficient by Landreth and Adrian [9], for the entire vector field. If there are still a number of apparently erroneous vectors then these vectors are re-calculated with an enlarged reference matrix (from 5 x 5 to 30 x 30). If an alternate or "preferable" vector results from this re-calculation, then it replaces the previous vector. The re-calculation can be repeated a number of times to "correct" the remaining erroneous vectors.

The inner workings of the cross-correlational technique using the DSP housed in a computer are described in Appendix A.

2.2 Image Capturing

If the images are recorded onto a video tape-recorder (VTR) at a normal speed of 30 frames-per-second (fps) the characteristic time of motion is limited to 1/30th of a second. When the shortest characteristic time of motion in the field of interest is slower then 1/30th of a second (33.33 msec), then the normal framing rate may be adequate. If however, one expects shorter characteristic times the normal framing rate becomes an operationally limiting factor. In this case one can take advantage of CCD cameras that can operate in a charge interlace mode; that is, since the camera acquires first the odd field and then the even field, the time interval is halved to 1/60th (16.67 msec) of a second. If the laser light source can then be pulsed at 1-10 msec intervals, the first two images are acquired using only the even field and the subsequent two images using the odd field. Figure (Appendix) A-1 depicts this schematically with a pair of even and odd fields representative of a CCD array. In the schematic then the vertical lines represent the laser pulses. By this method then the time interval between light pulses is no longer controlled by the camera's framing rate. Of significance with this shorter interval is the ability to track higher shear rate flows. However, as the displacements between the reference and corresponding matrices become shorter the accuracy of the calculated velocities decreases. In order to counter this influence, in essence to compute the displacement with sub-pixel accuracy, Kobashi et al. [10] for example used an Gaussian fitting method in order to assess the maximum location of the cross-correlation functions. Other techniques regarding accuracy, precision and image capturing in PIV are for example discussed in [11].

2.3 Laser Induced Fluorescence (LIF)

Although in principle the illumination of the tracer particles within a flow field of interest by a laser sheet or by other means is sufficient for data acquisition in PIV, depending on the flow phenomena enhancement of the light intensity from the tracer

particles with respect to the rest of the flow field may often be needed in terms of the "quality" of images on which one applies correlation methods. One commonly applied technique is Laser Induced Fluorescence (LIF). LIF is an experimental technique used in conjunction with PIV which enables the user to, in principle, measure the velocity, temperature and concentration fields simultaneously. The fluorescence properties of the tracer particles themselves, as induced by laser light, is used to act as point light sources in the recorded images. This is in addition to reflectance of the laser light by the particles themselves. Thus while unwanted reflectance, for example from surfaces in the flow field, may overwhelm (saturate) the CCD camera captured images with respect to the tracer particles, implementation of LIF along with PIV regains some of the contrast between particle and background where saturation is not a problem. A further description of LIF for use in PIV and for temperature field measurement is given in Appendix B.

2.4 Visiflow and Photocam

While in the example application of PIV described below, a software package developed at Keio University was used, a commercially available PIV data analysis package called *Visiflow* has been implemented at PNC. Visiflow is a fully-automated PIV image analysis software package developed by AEA Technology at the Harwell Laboratory in the UK [12]. The package is able to extract quantitative information from multiply imaged PIV "records". The software operates on a DOS (or DOS-J) based PC platform under a Windows environment.

In addition a Photron PhotoCam CCD camera similar to the one used by Keio University has been installed at PNC along with the Visiflow software [13]. It is the authors intentions to implement the PIV system for the second phase of tests of the Thermal Striping experiment [5], which in addition uses ultrasound Doppler velocimetry. After gaining valuable experience in the present work, it is planned to validate the two independent velocity measurement methods with one another.

3. Example Application

3.1 Introduction

The study of flow around a solid body such as a hemisphere or that around a single gas bubble rising in a volume of liquid are two *classic* examples of problems in fluid mechanics of multi-phase flows. It goes without saying that our understanding of such rudimentary systems can be and is often extrapolated and applied to larger scale systems such as fluidized-beds, bio-reactor bubble columns and other equipment involving solid-liquid and gas-liquid flows. Our base of knowledge on the fundamental aspects of these types of flows amassed over many years are contained in such texts as by Levich [14] and Clift et al. [15]. We know that the accumulated knowledge, experimentally has been inspired by observation and operation of real engineering systems. Experiments are thus and have been an indispensible part of these investigations.

With regard to velocity measurement techniques employed in past experimental investigations, they mainly encompass a wide variety of (*classic*) flow visualization techniques and pointwise measurement by such methods as hot-film/hot-wire and laser Doppler anemometry. Owing to the importance of fluidized-bed technology, a number of experiments have studied the flow of solid particles around a gas bubble in a solid-liquid-gas system.

In the present work we first sought to apply a number of *recent* measurement techniques (in contrast to the *classic*) in unison to the fundamental problem of flow around bubbles and in this case, its corresponding solid counterpart. Our objectives were thus two-fold: 1) to explore the applicability of DPIV, LIF and a specifically developed shadow technique to this problem and 2) to evaluate the information content produced by our measurement system; that is, measurement of the differences between flow around a solid and a bubble.

3.2 Experimental Apparatus

In order to detect the interaction between the bubble motion and the turbulent flow field around it we implemented a Digital Particle Image Velocimetry (DPIV) system previously described by Sakakibara et al. [16,17]. Our original intent was to simultaneously capture both the bubble and tracer particle motions, the latter of which was approximately 1000 times smaller in size than the bubble. However, it became clear that the intensity of light reflected from the bubble's surface saturated the CCD camera such that the intensity of light from the tracer particles was overwhelmed. We thus resorted to application of Laser Induced Fluorescence (LIF) using fluorescent particles (1-10 μm) with a specific density 1.02 along with a light-sheet produced by a argon-ion laser; that is, by mixing these particles with rhodamine-B we could detect the fluorescence emitted by the particles through a color filter (to cut reflections) into our CCD camera. We found that with this set-up we could detect the motion of tracer particles in the vicinnity of the bubble-liquid interface.

Next in order to measure the bubble's shape we supplemented the DPIV-LIF system with an infrared shadow-image technique (IST) specifically prepared for this experiment. Figure 3 thus depicts our arrangement consisting of two CCD cameras; one for DPIV-LIF (rear camera) and the other for IST(front). A shadow was produced from infrared LEDs outlining a square and located behind the bubble. The emitted light was filtered through a translucent cover-sheet and produced a shadow of the bubble (or solid) onto the CCD camera. In order to capture both the bubble shape and the flow field around it we synchronized the triggering of both the laser and the LEDs.

As for the experimental apparatus it consisted of two rectangular tanks, a lower and upper, connected in between by a vertical, channel of $100 \times 100 \ mm^2$ and 1000 mm in length. A schematic is shown in Figure 4. At the top of the channel there is a entrance section with a grid in order to generate a homogenous incoming flow. The test medium was water and flowed freely down through the channel to the lower tank where it was pumped back up to upper tank. The mid-region of the channel was our measurement section and consisted of a port from where either a bubble or its equivalent solid could be introduced. The bubble or solid was attached to a small disk

(dia. ~ 2 mm) located at the end of a needle suspended across the channel by a piano-wire. We note that in the case of the bubble it was thought that the surface tension kept the bubble attached to this small disk even as water flowed downward. The operational flowrate was held constant at U_{avg} = 0.245 m/s while the corresponding turbulent intensity level due solely to grid-generated turbulence was ~5 % in the channel. This level was measured separately by laser Doppler velocimetry. As for the reference bubble size used in the presentation of our data, we used the breadth of the bubble D = 12 mm. This figure was supported by a calculation of the breadth from a correlation put forth by Tadaki and Maeda [18] based on the flow and physical properties.

4. RESULTS

4.1 PIV results

Figure 5 shows a representative still image of the bubble's shadow (in black) imposed on a grayscale background. The bubble in the figure is *right-shifted* in a descriptive sense and has been captured at one instant of a continous oscillatory motion in all three axial directions. The bubble is attached at the top (center) to a small disk that is marked by a white dot within a black region. Figure 6 depicts a representative image of the tracer particles, including a partial outline of the bubble boundary and the region inside which contain fewer speckles. Note especially in the latter figure that there is a *white-out* region located at the top. This appears to be a region of high light reflectance resulting from, in general, the bright laser light and multiple reflections from various surfaces.

Based on these and similar images for the equivalent solid, we extracted velocity information from a collection of more than 1000 images. Other velocity-related information were subsequently calculated. For initial comparison, we present in Figures 7 and 8 an enlarged section of the measured flow field around the bubble and solid. In the figures the laser sheet enters from the left and introduces a region of relatively larger uncertainty with respect to the calculated vectors to the right of the solid or bubble; that is, due to total and partial shading respectively in the cases of the solid and bubble, the error in this right region is higher relative to the rest of the field. We henceforth will show data from only the left side of the measured flow field. As for differences in their respective flow fields, upon close scrutiny we note that the flow pattern and the spatial extent of flow in the wake regions are different; that is, in the case of the solid there is a longer wake region and recirculating flow area in comparison to the bubble. Of course the non-slip boundary condition at the solid's surface and the slip condition at the bubble's surface influences this wake flow. The generation of vorticity at some separation point along the edge of their respective boundaries, the conveyance of vorticity along the nearby free shear layer, the formation of a circular vortex (two-dimensional) or vortex ring (three-dimensional) and eventual shedding of vortices by an entrained cross-flow are nevertheless common mechanisms in both the solid and bubble. However, since the bubble oscillates substantially with the flow, there is also a contribution from this motion (to the flow field); that is, it is likely that turbulence is generated from the oscillatory motion of the bubble whereas it is not in the case of the solid.

Figure 9 thus shows the cross-stream distribution of the average (U/U_0) and normalized RMS (u_{rms}/U_0) velocities respectively to the left and right of the figure. Here U_0 represents the average velocity without bubble or solid as measured by LDV. To facilitate our discussion, 4 axial locations close to the solid and bubble and 2 locations further away $(x/D = 1.08, 3.25)$ have been selected. To the authors' knowledge, velocity measurements at less than a diameter's distance in the wake region of a bubble are rare. In each of these figures the blank and filled circles represent respectively the bubble and solid data. Note that although the *on-average* velocity defect is slightly larger for the bubble at close range $(x/D < 1.08)$, u_{rms}/U_0 has a larger variation and extends further downstream for the solid. The data at $x/D = 3.25$ essentially shows that flow is identical for both flow parameters at this downstream location. In **Figure 10 and 11** we show the corresponding cross-stream average (V/U_0) and normalized RMS (v_{rms}/U_0) velocities. Whereas one-half of symmetric distributions in Fig. 9 were shown, the full profiles are shown for later comparison with ultrasound Doppler velocimetry data. In fact, due to the bubble's oscillatory motion notice that V/U_0 and v_{rms}/U_0 are generally larger for the bubble in contrast to the solid.

While Figs. 9 and 11 show relative magnitudes of u_{rms} and v_{rms} with rrespect to U_0 **Figure 12** shows a direct comparison of the RMS values along the streamwise direction with the cross-stream direction as parameter. Note that except at the centerline for $x/D < 0.85$ the bubble's oscillatory motion again contributes to a consistently larger v_{rms} than the solid. On the other hand the reversed flow just along the centerline typically appears to show as much as 4 times more fluctuation in the case of the solid in contrast to the bubble. In other words the cross-stream flows are spatially confined behind the solid in comparison to the oscillating bubble.

The data presented thus far show averaged quantities calculated from a multiple number of images. While these figures provide some insight, details of the flow field as dictated by the bubble's motion is overlooked. We thus present in **Figures 13 and 14** a sequence of vector field plots, respectively with the identified bubble's shadow image and that of the solid superimposed at 50 ms intervals. The sequence which was recorded with a normal speed (30 fps) CCD camera, although clearly depicts the change in shape and position of the bubble, only captures snapshots of the bubble's continuous oscillatory motion which we judged to be approximately periodic every 200 ms. Note the change in the flow field with respect to the bubble's position at each 50 ms interval. In fact upon close scrutiny of the vector field in the figure, one can approximately identify the formation and shedding of the vortices. Notice that the shedding is not necessarily at the spatially extreme (right or left) positions of the bubble.

Figure 14 shows a similar sequence for the solid. Notice that here that the *body* is consistently identified in shape but, also exhibits some sideways motion most easily detected with respect to the outline of the square measurement area. Although this motion may influence the solid's wake velocity field, we observed that in comparison to the bubble the oscillation frequency was much smaller and in addition thought the deformation of the bubble-shape would strongly influence its wake flow-

field. In fact, because the bubble shape does change so drastically in time, we selected four representative *types* of shadow images from the sequence shown in order to selectively study its corresponding flow fields. We show these four types (type 0, 1 2 and 3) in **Figure** 15 and note that they typically represent the time events in Figure 10 as follows: 1) type [flat] 350 ms, 2) type 1 [left-shifted] ~ 400 ms, 3) type 2 [right-shifted] ~ 300 ms and 4) type 3 [full] ~ 250 ms. The word in brackets gives their short descriptive names.

We next show in **Figure 16** the vorticity contours contras-ting the bubble and solid. The sense of positive and negative vorticity are noted respectively by solid and dotted lines. One can see that besides the nearly symmetric distribution of vorticity about the central axis for both the bubble and solid, the contrasting feature is the large vorticity values in the case of the bubble. Since large velocity gradients, typically from free shear and vortical flows, are known to have large vorticity the distribution as shown is at least qualitatively consistent with the vector field plots comparing bubble versus solid in Figs. 13 and 14. Next in **Figure 17** we show the vorticity contours corresponding to the four bubble types shown in Fig. 15. Note here that the left (type 1) and right (type 2) bubble orientations distort or respectively "pinch" the otherwise symmetric (type 0 and 3) vorticity distribution. The concentration of vorticity, however, from the unspecified separation point just aft of the bubble does not appear to change in location.

In **Figures 18** and 19 we display the turbulent energy distribution contours corresponding to Figs. 16 and 17; that is, at first contrasting the bubble/solid and subsequently, for each of the four selected bubble types. The turbulent energy is here defined as $k = 1/2 \, (u'^2 + 2 \, v'^2)/ U_0^2$ as v' and w' have been assumed to be equivalent. Note that once again the contours are generally similar in shape but, not in detailed trends nor in magnitude. In fact, although the bubble appears to generate more vorticity than the solid (Fig. 16), the turbulent energy is not analogously distributed. In fact, the energy is certainly evenly distributed in the case of the bubble in comparison to the solid. This is clearly indicated by the contours for the four types where right and left orientations show equally shifted energy distributions.

Finally in **Figures 20** we depict the spanwise profiles of, respectively, the turbulent kinetic energy and Reynolds stress of the bubble and solid at the same streamwise locations as previously shown data. Note that consistent with Figs. 16 and 17 the Reynolds stress for the bubble shows a peak at $y/D \sim -0.5$ $(x/D < 1.08)$ while for the solid a peak doesn't appear until $x/D = 1.08$. Again at $x/D = 3.25$ there is no difference between the two.

4.2 UVP results

As a matter of comparison and partial validation, a limited series of velocity measurements were made using the ultrasound velocity profile monitor (UVP). We have previously described the UVP as working on the principle of Doppler echography [19]. In the present case the UVP Model X-3 was used with a single transducer operating at 4 MHz. A total of 1024 velocity profiles, each containing 128 points are taken during a measurement span. Measurements were made from the side

so that given U = (u,v,w), we measured the v-component of velcity in the wake region behind a single bubble. Since the wall thickness of the acrylic test section was 11mm thick we expected and experienced attenuation of the ultrasound wave. We did manage to record a velocity profile however, so that we proceeded with measurements.

In Figure 21 and 22 we show the average velocity (v-component) with distance downstream of the bubble as parameter. The former figure shows the overall change in profile over the measured range, while the latter shows the drammatic change in the profile between $10 < x < 14$. We then show in Figures 23 and 24, the standard deviation distribution associated with the average velocity at similar different downstream locations. Notice that in the latter figure a change in the profile takes place between $6 < x < 10$.

We then show in Figure 25 the average velocity and the maxima (maximum and minimum) at downstream distances from the bubble. Since the bubble is oscillating we expect the average velocity to approach 0 mm/s if the facility is upright and the flow in the channel is symmetric. We see that this is indeed the case except for $x < 10$ where we need to inspect the maxima closely. Note that particularly at $x \sim 6$ the flow is directed toward the transducer (maximum) while the minimum is approximately zero. The maximum then decreases due to the influence of flow away from the transducer (minimum). This explains the decrease in the maximum beyond $x \sim 6$ and qualitatively verifies the oscillation-induced flow in wake of the bubble.

Finally in Figure 26 we plot a contour of the turbulent kinetic energy just based on the v-component of velocity, (v'^2 / V_{avg}) where v' is the standard deviation associated with the average. One can see that consistent with Fig. 25 there is a concentration of energy between $6 < x < 8$ ($57 < ML < 67$) and therafter a more or less symmetric distribution about the centerline roughly located at $ML \sim 60$.

5. DISCUSSION

The results as presented appear to fulfill much of our first objective; that is, the combined use of DPIV, LIF and the above-described infrared shadow technique enables one to identify both the shadow of a body and the flow field around the body simultaneously. In addition, based upon close scrutiny of the measured velocity vector field and subsequent velocity derived plots, we are able to elucidate and verify a number of phenomenological facts regarding the differences in the wake flow produced by a bubble and a solid.

First in order to facilitate our discussion, we refer to Fan and Tsuchiya [20] (hereafter written F&T) who describe in detail many of the physical mechanisms observed in this experiment regarding the bubble and its wake flow field. If we use for instance the observed breadths of the bubble (b) and average channel velocities (U_{avg}), the estimated bubble Reynolds number ($Re = U_{avg} b/v$) range is 1800 to 2700. Note that contrary to most experiments where the bubble rise velocity is measured, we have an oncoming flow toward a *fixed* bubble. With an estimate of the Reynolds number, we see from a plot of past experimental data of Strouhal ($Sr = f_{osc} b / U_{avg}$; f_{osc^-}

frequency of oscillation) versus Reynolds numbers [F&T] that our corresponding Strouhal number for vortex shedding is approximately 0.15 to 0.20. A equally separate calculation of the Strouhal number based on an estimate of the bubble's oscillation frequency from high-speed video images yields $0.16 < Sr < 0.245$. The oscillation frequency from high-speed video-images were estimated visually and at present could not be resolved to better than 4-6 Hz. This then roughly confirms the proper range of the relevant mechanisms.

Although the details of the vortex shedding mechanism especially for a bubble are of great interest, due to the great difficulties in direct measurement, most of the experimen-tal evidence has been accumulated from photographic and visualization techniques that are non-intrusive in nature. In reviewing this data F&T assert that the wake flow behind a bubble is characterized as follows: 1) the bubble tends to oscillate in order to reduce its wake size; 2) by reducing its wake size the bubble also minimizes the pressure loss behind the bubble and thereby its drag; and 3) this reduction in wake size is best realized when the vortex shedding and bubble oscillation frequencies are near unity.

In other words in comparison to the solid, the bubble's oscillatory motion generally serves to minimize the energy loss while rising through the liquid phase or in our case as the water flows past it. It is therefore not surprising to see in **Fig. 18** that the iso-contours are less densely spaced for the bubble. The turbulent kinetic energy is evenly distributed throughout the flow field for the bubble whereas the iso-contours for the solid are more densely spaced. The overall shape of the iso-contours as well as the order of magnitude of the turbulent energies are, however, similar for both objects. This latter result may be slightly surprising since typically the production of turbulence is concurrent with large Reynolds stresses and strain fields. From Fig. 20 (right) it is clear that at distances less than a diameter, the bubble has a larger Reynolds stress in the vicinnity of y/D ~ -0.5 than the solid. An equally large stress does not appear for the solid until x/D = 1.08. These trends are consistent with the spatial distribution of vorticity in Figs. 16 and 17. Fig. 20 then leads us to believe that inspite of the aforementioned contrasts, since the turbulent kinetic energies are roughly equal, flow around a solid versus that around a bubble must have inherently different energy dissipation mechanisms. It is also reasonable to believe that part of this dissipation is within the internal flow (air) of the bubble.

Finally, concerning the identification of the shadow-image boundary, the identification is complicated by the oscillatory motion of the bubble in all axial directions; that is, owing to this motion, the bubble distorts its own shadow in both the x-y plane and in the z-direction relative to the LED-array. We have thus taken an average of many images in the bubble shapes shown here. Furthermore, the identification of the boundary is partially subjective in that while the location of the disk and the approximate size of the bubble (in this case 12 mm) in the CCD camera's field-of-vision is known (since it is fixed), the identification of the bubble boundary itself is aided by discrimination of DPIV-produced vectors; that is, the discrimination of *real* and *unreal* vectors corresponding to vectors in the flow field and those erroneously represented. These erroneous vectors were in most instance, those located within the bubble, a physical impossibility. If all the contributing sources of error

were to result in a one or two pixel per identified boundary uncertainty, the total error as a fraction of cross sectional area has been estimated to be in the range 15 to 25 %.

5.1 PIV versus UVP

Only a limited comparison of PIV and UVP data can be made since only the v-component of velocity has so far been measured by ultrasound Doppler velocimetry. Some comparisons, namely the average velocity, *rms*-velocity and turbulent kinetic energy, can nevertheless be made. To begin a comparison of Figs. 10 (a and b) and 21(22) reveals a similarity in velocity profiles with downstream distance. Note that in Fig. 10 the positive and negative scales are inverted so that when corrected the negative and positive portions of the profile appear respectively left-of-center and right-of-center. Then between $0.67 < x/D < 0.75$ in Fig. 10 and analogously $10 < x < 14$ in Fig. 18 there is a transition in the profile; that is, the profile is inverted about the horizontal axis as one proceeds downstream. Since this particular transition was identified by two independent measurement methods, there is strong evidence that phenomenologically there is a "near" wake region and a "far" wake region behind an oscillating bubble.

The *rms*-velocity in Fig. 11 and standard deviation profile in Fig. 23 and 24 are on the other hand less similar than the average velocity. While v_{rms} is slightly peaked in the central, right- and left-most regions in the near wake in Fig. 11 ($x/D < 0.83$), the standard deviation profile is highly peaked and changes markedly from $x=4,6$ to $x=8,10$. It stands to reason that (beyond $x=10$) the velocity fluctuations reveal themselves in a Gaussian-like, symmetric distribution in the central region. And consistent with the average profiles, there is a transition from the near to far wake. The specific profile at $x=4,6$ however, are difficult to explain especially in the region $ML > 90$ where large magnitudes are reached. This will be further investigated.

As for Fig. 25 we already mentioned that since the flow in the wake is approximately symmetric, we expect the average velocity to be near zero and for the maxima to balance in magnitude. This is indeed the case in the figure except for $x \sim 6$ where there is flow away from the transducer. This indicates that "on-average" there is a large cross-stream (tranverse) flow in a narrow region of the wake. By "on-average" we mean the time span over which we averaged the velocity. We are of the opinion at this time that further measurements are needed in order to validate this phenomenom. If the system is balanced as it seems, it is difficult to imagine a preferential cross-stream flow in the wake.

Lastly Fig. 26 verifies rather qualitatively, since only the v'-component was measured, that the turbulent kinetic energy distribution in the wake is approximately symmetric; that is, beyond $x \sim 8$ the "patterns" appear symmetrically to the imaginary centerline at $ML \sim 60$. Recall that the bubble is roughly centered at $ML \sim 60$ along the ordinate axis. In between $6 < x < 8$ however, there is a relative concentration of energy which we identified as the near-wake. We referred to the region beyond this as the far-wake. Note also that near the outskirts (top and bottom regions) the energy distribution is similar as well. Since we presented in Figs. 18 and 19 the PIV-derived

distribution which includes both u- and v-components, we can only draw qualitative conclusions from this figure.

6. CONCLUSIONS

Although ultrasound Doppler velocimetry has proven itself to be a versatile velocity measurement tool in thermal-hydraulics, when afforded the opportunity for data validation by a second velocity measurement method, we would like to establish the relevance of both techniques. In the present case, we have chosen Particle Image Velocimetry as our second, independent means for velocity measurements. PIV can be applied to gas and transparent liquid flows (in our case water) and relies heavily on modern image processing technology and laser light illumination of the flow field of interest. When applied to 2D velocity fields (3D possible) it can produce roughly the same order of magnitude number of vectors as commonly seen by numerical methods. The method in this respect is the perfect bridge between numerical fluid dynamics produced results and 2D (and 3D) measurements now underway by UDV. UDV can be used opaque fluids and potentially sodium. In the present report we introduced the PIV methodology and systems set-up, as well as a basic application in wake flow behind an air bubble suspended in downward flow of water in a vertical channel. The example application, though simple, has many similarities to jetting, oscillating (vibrating) and wake type flows and thereby demonstrates the applicability of PIV.

Thus using DPIV, supplemented by LIF and an infrared shadow-image technique (IST) produced by an array of LEDs shining through a translucent window, two CCD cameras were use to simultanouesly identify the boundary (shape) and flow field around a bubble and its corresponding solid equivalent. The bubble or solid was suspended in the middle of a square channel in which water flowed downward through a grid arrangement. From a collection of more than 1000 images, boundary and velocity information were extracted. A comparison of first the vector flow field around the solid and bubble revealed differences in the wake flow structure as expected; that is, the implemented measurement system was able to detect differences in the flow field resulting from, respectively, the non-slip surface boundary condi-tion in the case of the solid versus the slip condition at the bubble-liquid interface for the bubble. We additionally noted that the oscillatory motion of the bubble appeared characteristic under the given experimental conditions. Upon scrutinizing the average velocity, RMS-velocity, u and v RMS ratio, vorticity and turbulent kinetic energy contours and finally the Reynolds stress distributions, we noted that indeed the bubble's motion locally produces regions of large Reynolds stresses but spatially distributes the generated turbulence much more evenly than the solid.

Lastly, the beginnings of a comparison with UVP measurements was introduced. It is expected that more measurements will be taken in the future. The results to date of the v-component appears to partially validate the PIV measurements; that is, the average velocity trends are similar. The standard deviation trends are however, less similar and only further investigations will resolve the uncertainties.

Both the UVP and PIV velocity measurement techniques will be used in thermal striping experiment and in the Interwrapper Flow experiments.

Nomenclature

D: Equivalent diameter of bubble or solid object

ML: Measurement Length, refers to UVP measurement length

Re: Reynolds number

Sr: Strouhals number

U_0: Average velocity at the entrance of test section

U, V : Downstream and cross-stream velocity

u_{rms} , v_{rms} : Root-mean-square velocity components

u', v' : Fluctuating component of velocity

X: Downstream (axial) distance down the channel

Greek Symbols

ρ: density, [kg/ m^3]

ν: kinematic viscosity, [m^2/s]

References

[1] Y. Takeda, Velocity profile measurement by ultrasound Doppler shift method, Int. J. Heat and Fluid Flow, vol. 7, 313-318, 1986.

[2] Y. Takeda, Development of an ultrasound velocity profile monitor, Nucl. Eng. Design, vol. 126, 277-284, 1990.

[3] Y. Takeda, Measurement of velocity profile of mercury flow by ultrasound Doppler shift method, Nuclear Technology, 79, 120, 1987.

[4] Y. Takeda, K. Samec and K. Kobayashi, Experimental measurement of 2D velocity vector field using ultrasonic velocity profile monitor (UVP), ASME FED-128, Experimental and Numerical Flow Visualization, 231, 1991.

[5] A. Tokuhiro, Investigation of free and forced flows of relevance to fast reactor thermohydraulics using the ultrasonic Doppler method, 1st International Symposium on Ultrasound Doppler method in Fluid Mechanics and Fluid Engineering, 9-11 Sept. 1996, Paul Scherrer Institute, Villigen PSI, Switzerland. To appear in Experiments in Fluids.

[6] J. Fox and A. MacDonald, Introduction to Fluid Mechanics, J. Wiley and Sons, New York, USA 1980

[7] J. S. Bendat and A.G. Piersol, Random Data: Analysis and Measurement Procedures, Wiley-Interscience, J. Wiley and Sons, New York USA 1971.

[8] F. Yamamoto, Y. Dai, M. Koukawa, M. Itoh and T. Uemura, Numerical simulation on error analysis in particle tracking velocimeter by correlation method, Proc. Flow Visuali1989, Winter annual meeting ASME, California, 9-14, 1989.

[9] C. C. Landreth and R. J. Adrian, Impingement of low Reynolds number trubulent ciruclar jet onto a flat plate at normal incidence, Experiments in Fluids, 9, 74-84, 1990.

[10] K. Kobashi, K. Hishida and M. Maeda, Measurement of fuel injector spray flow of I.C. engine by FFT based phase Doppler anemometer - An approach to the time series measurement of size and velocity, in Applications of Laser Techniques to Fluid Mechanics, R.J. Adrian, D.F.G. Durao, F. Durst, M. Maeda and J.H. Whitelaw eds., Springer-Verlag, Berlin Germany, 268-287 1990.

[11] R.J. Adrian, D.F.G. Durao, F. Durst, M. Maeda and J.H. Whitelaw eds., Applications of Laser Techniques to Fluid Mechanics, Springer-Verlag, Berlin Germany, 1990.

[12] Visiflow, Software for PIV analysis, AEA Technology , copyright 1987-96.

[13] Photron, FDMPCI- PhotoCam 120/60 CCD camera.

[14] V. G. Levich, Physicochemical Hydrodynamics, Prentice-Hall, Englewood Cliffs, NJ USA 1962.

[15] R. Clift, J.R. Grace and M. E. Weber, Bubbles, Drops, and Particles, Academic Press, New York 1978.

[16] J. Sakakibara, K. Hishida and M. Maeda, Quantitative visualization of convective heat transfer near the stagnation region of an impinging jet, Experimental Numerical Flow Visualization , ASME-FED-Vol. 172, 93-99 1993.

[17] J. Sakakibara, K. Hishida and M. Maeda, Measurement of thermally stratified pipe flow using image-processing techniques, Experiments in Fluids, 16, 82-96 1993.

[18] T. Tadaki and S. Maeda, On the shape and velocity of single air bubbles rising invarious iquids, Chemical Engineering, 25-4, 254-264, (in Japanese) 1961.

[19] Ultrasound Velocity Profile monitor (UVP) , Model X-3, Met-Flow SA, Lausanne, Switzerland, 1992.

[20] L.-S. Fan and K. Tsuchiya, Bubble wake dynamics in liquids and liquid-solid suspensions, Butterworth-Heinemann Series in Chemical Engineering, Boston USA isbn 0-409-90286-1 1990.

Acknowledgements
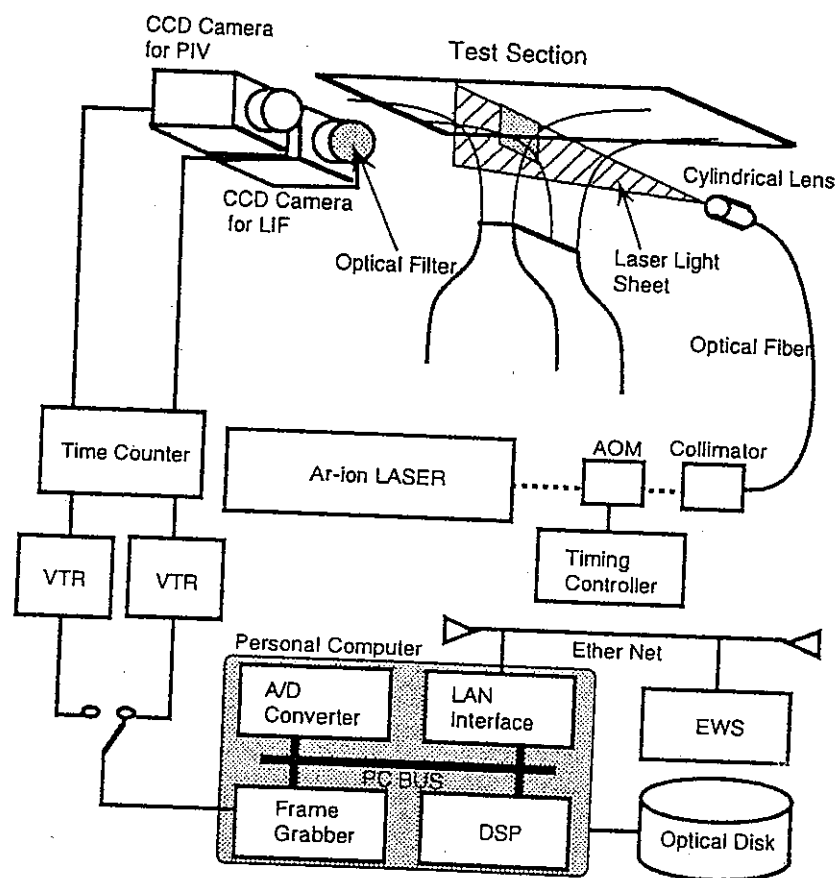
Figure 1. Functional schematic of a typical PIV system.
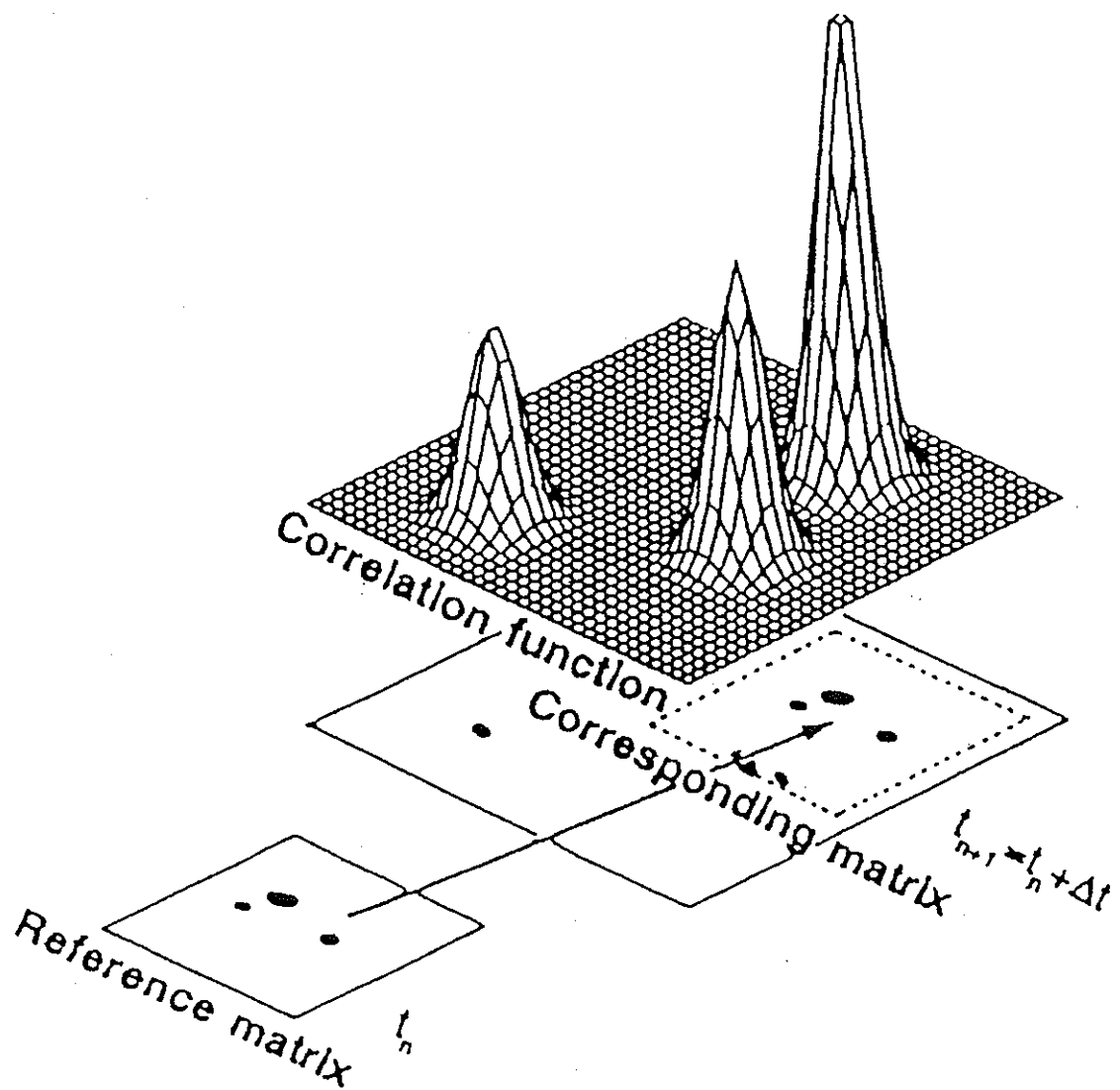
Figure 2. Principle of cross-correlation technique.
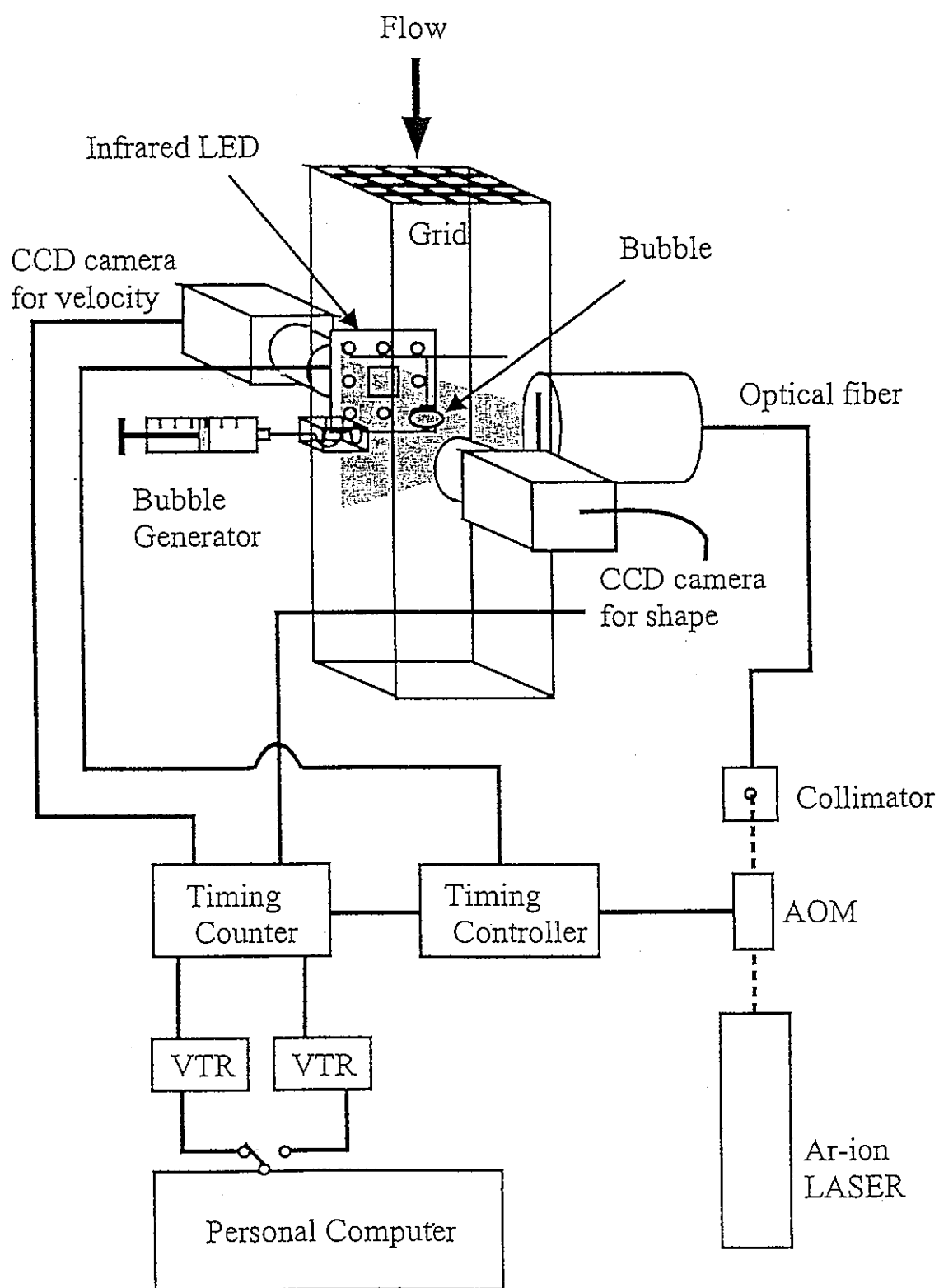
Figure 3. Schematic of measurement section with instrumentation.

1 Overflow Tank
2 Grid
3 Disk
4 Bubble or
    Solid Object
5 Bubble Generator
6 Tank
7 Pump

Overflow
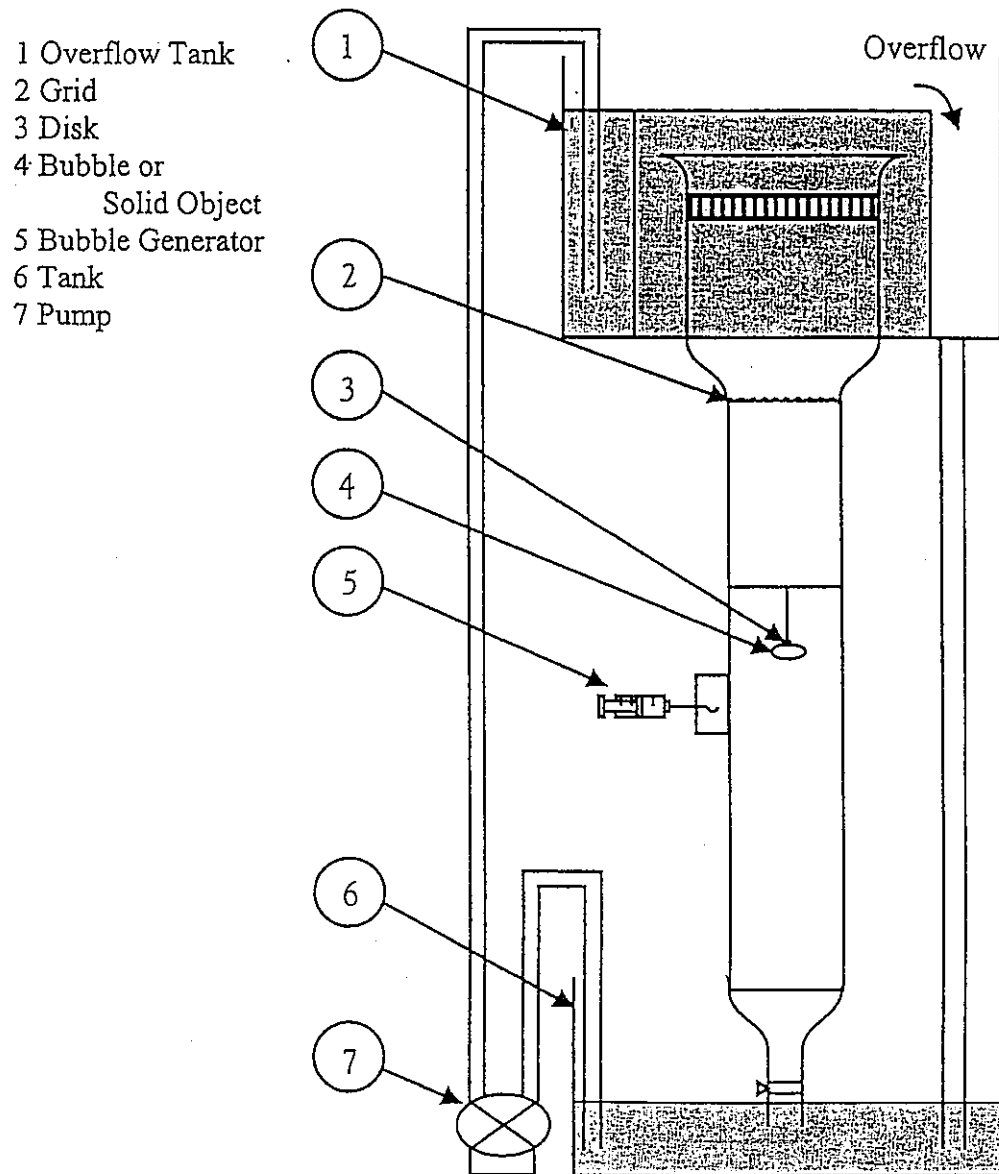
Figure 4. Schematic of experimental loop.
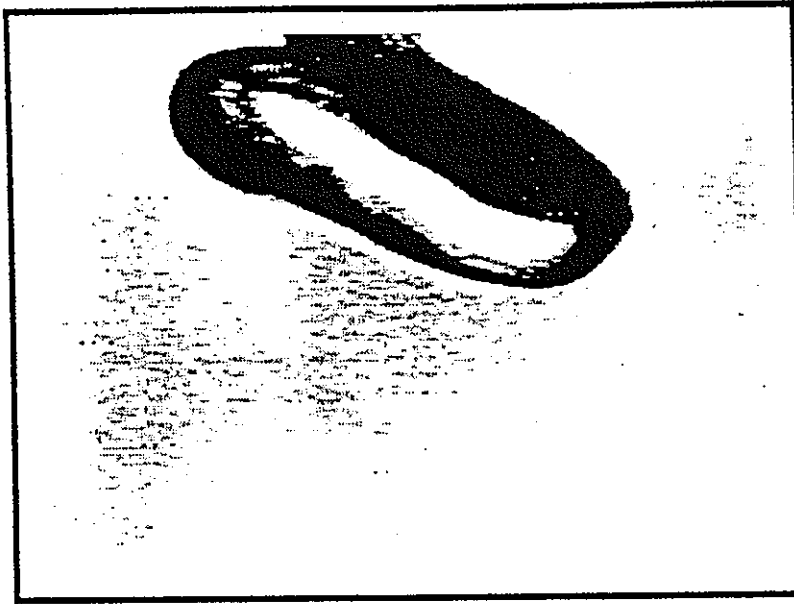
Figure 5. Typical shadow image of bubble as digitized from video.
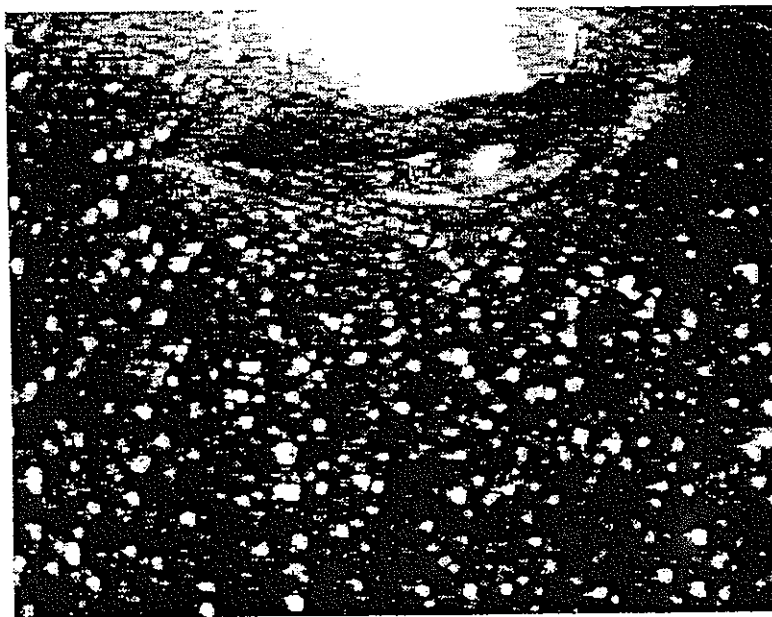
Figure 6. Typical particle image of flow around the bubble as digitized from video.
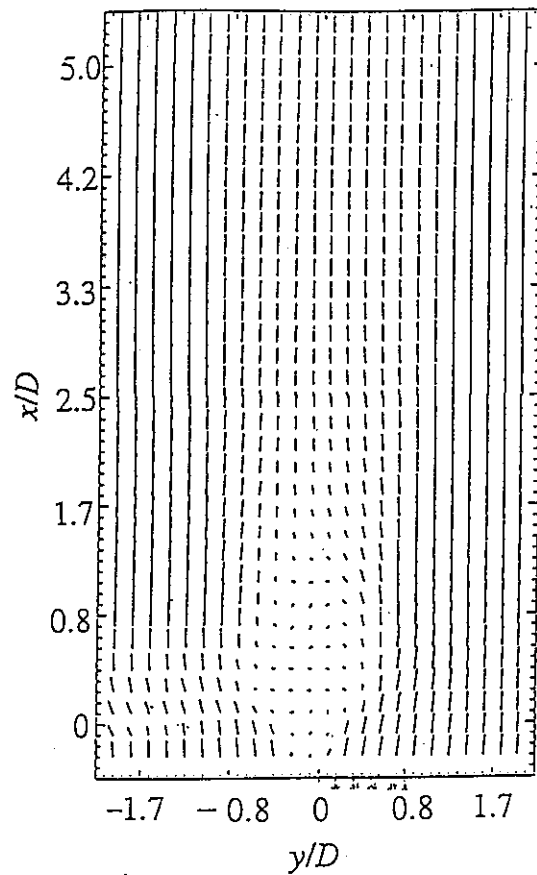
Figure 7. Representative vector field plot of the flow around the bubble.
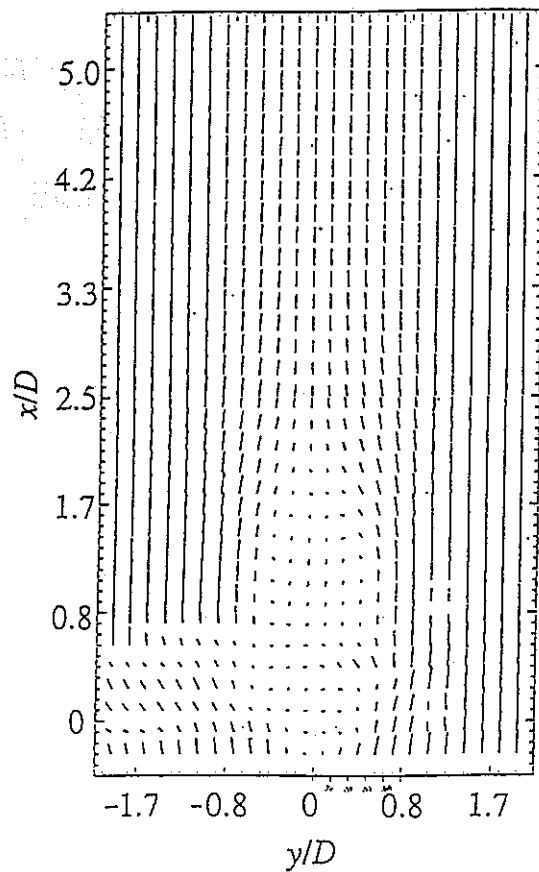
Figure 8. Representative vector field plot of the flow around the solid.
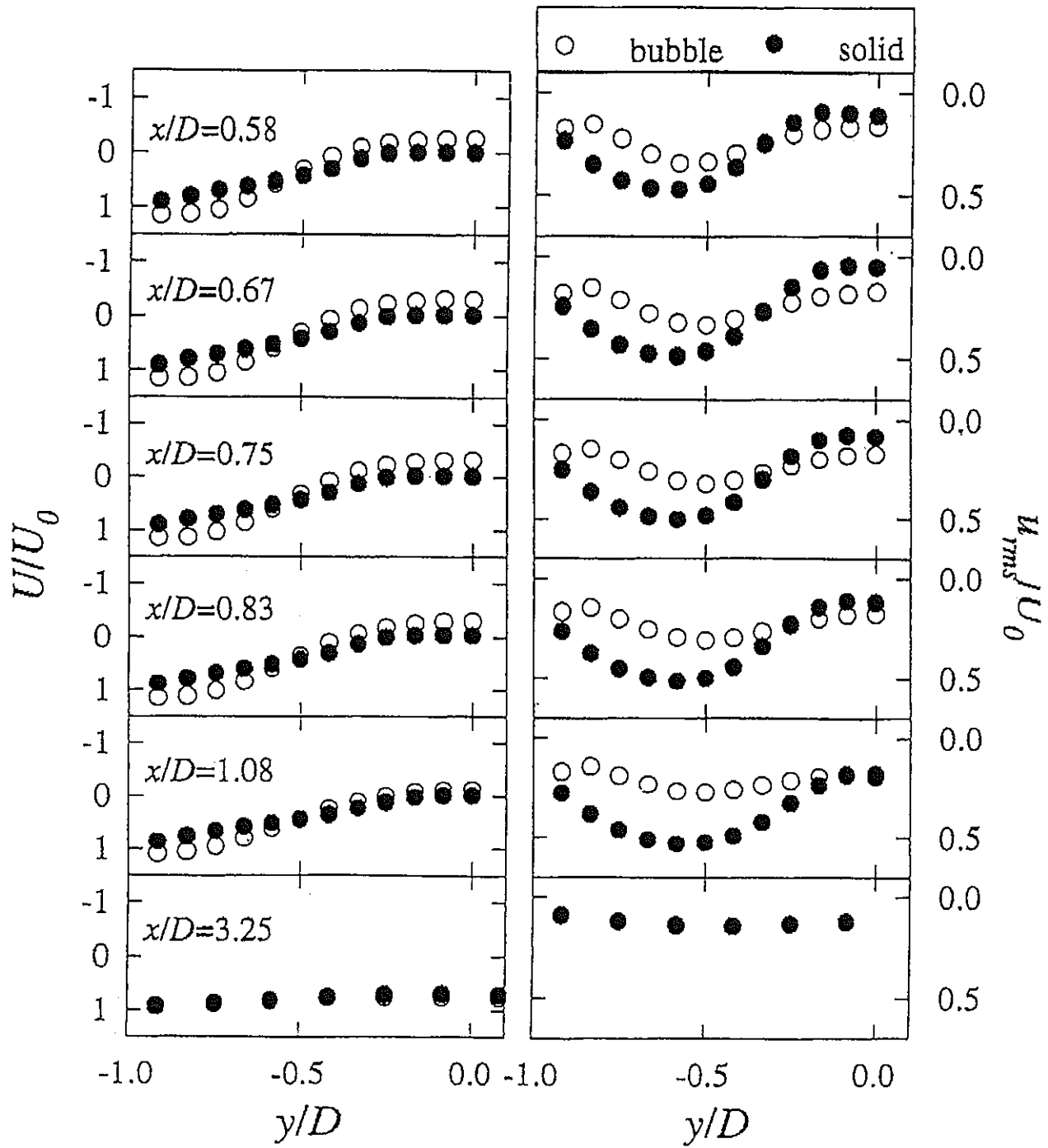
Figure 9. Streamwise variation of the average velocity and *rms*-velocity distributions. Only one-half of the profile is shown due to symmetry.
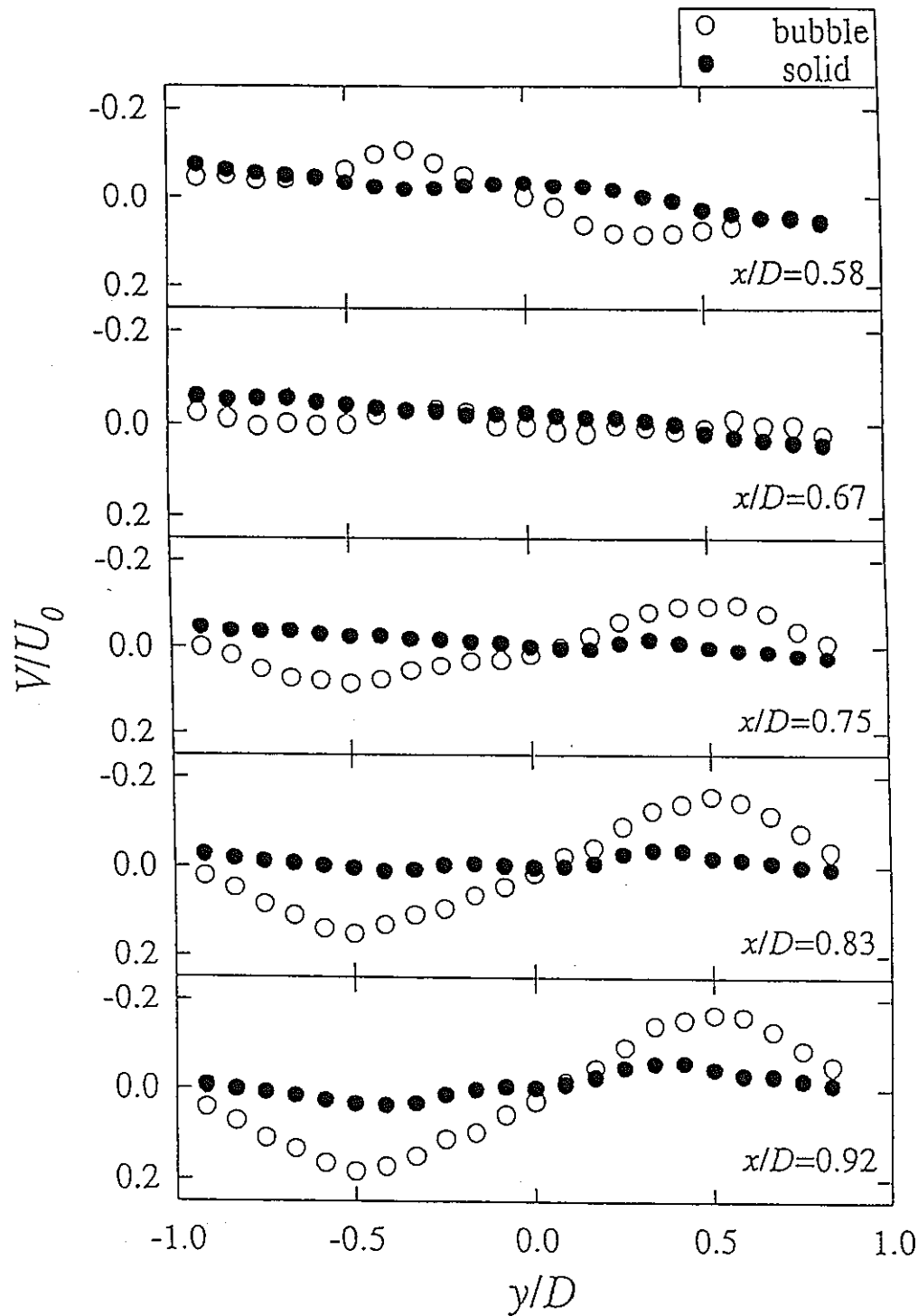
Figure 10 a. Streamwise variation of cross-stream average V/U_0.
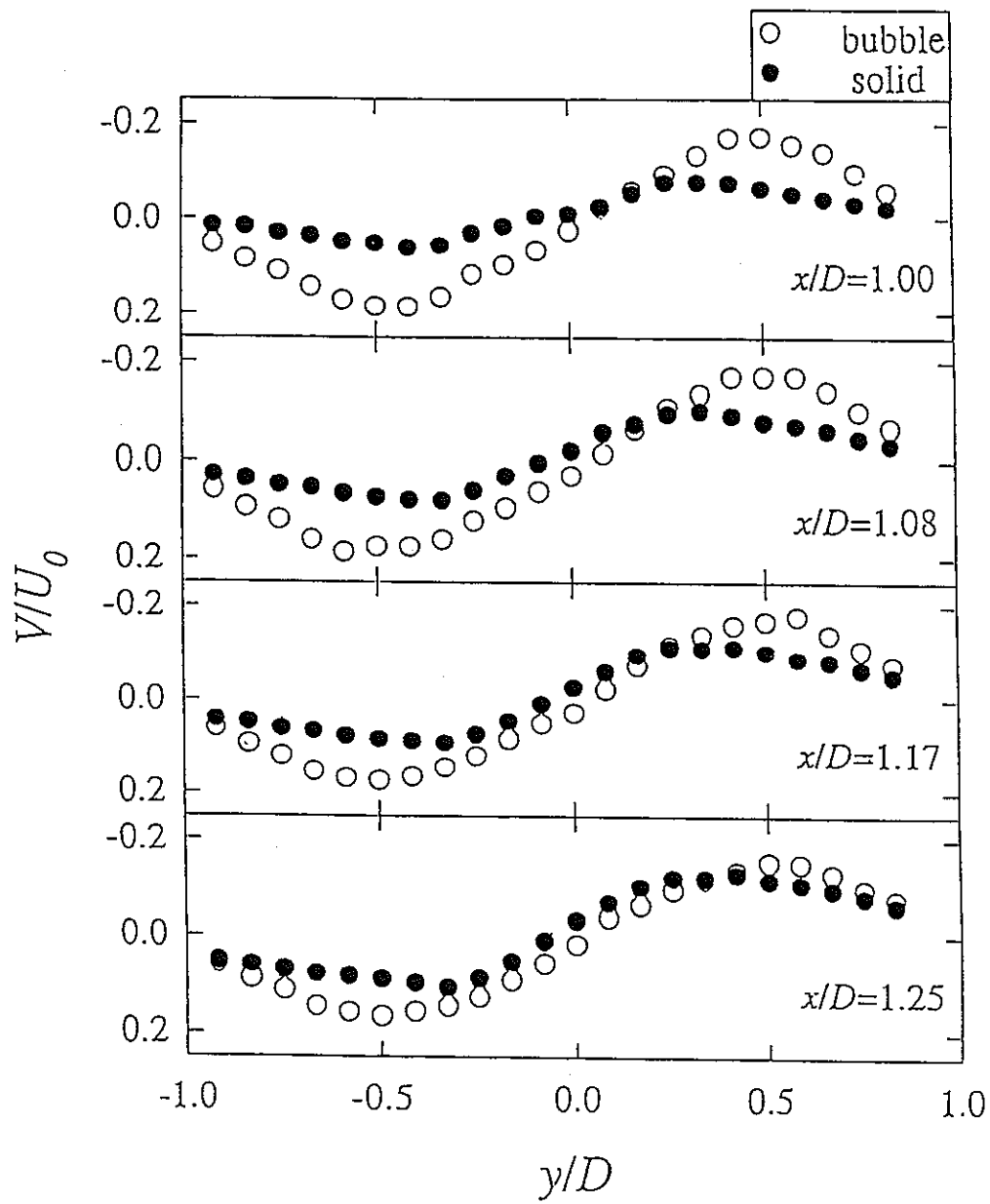
Figure 10 b. Streamwise variation of cross-stream average V/U_0.
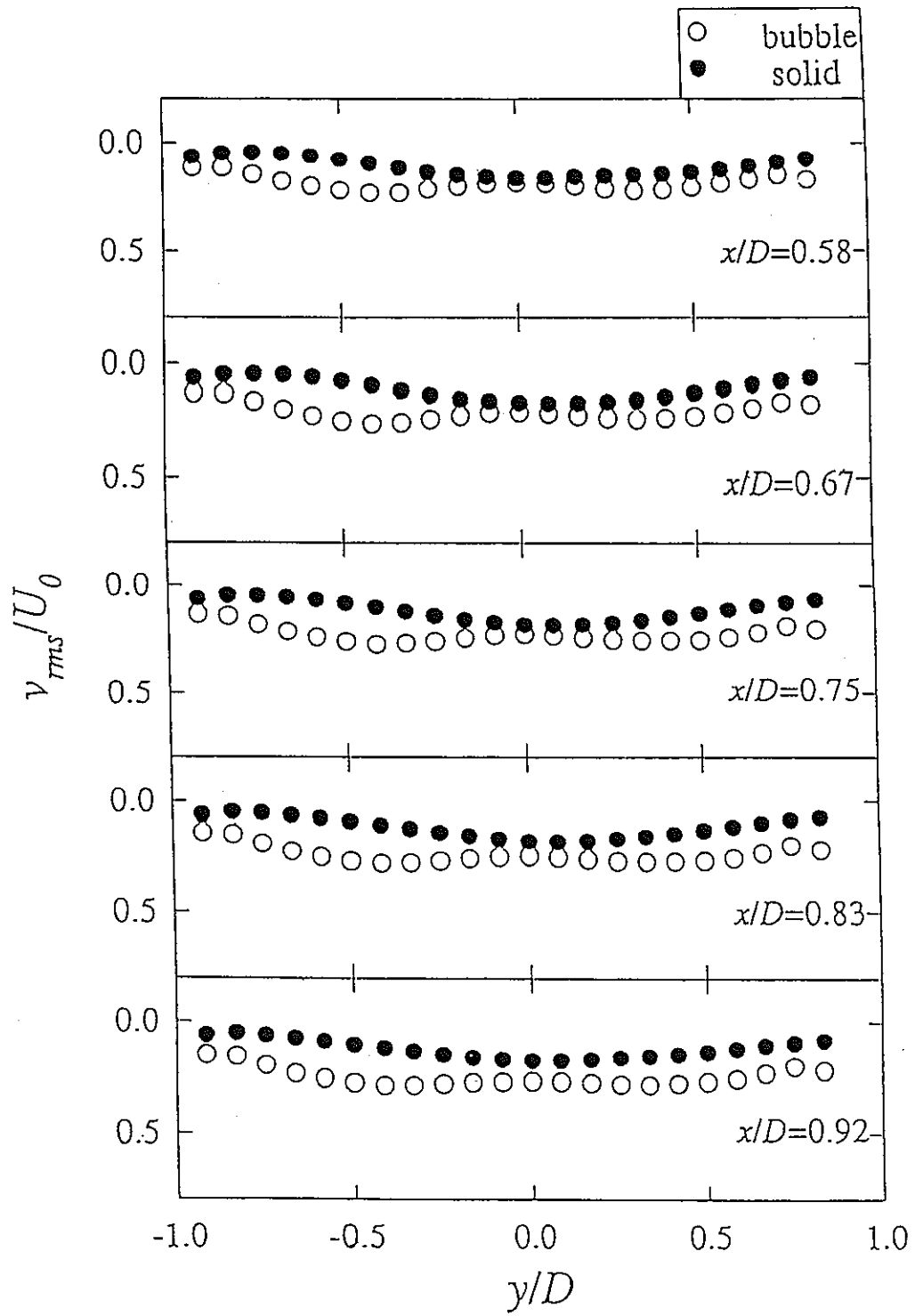
Figure 11 a. Streamwise variation of cross-stream rms-velocity v_{rms}/U_0.
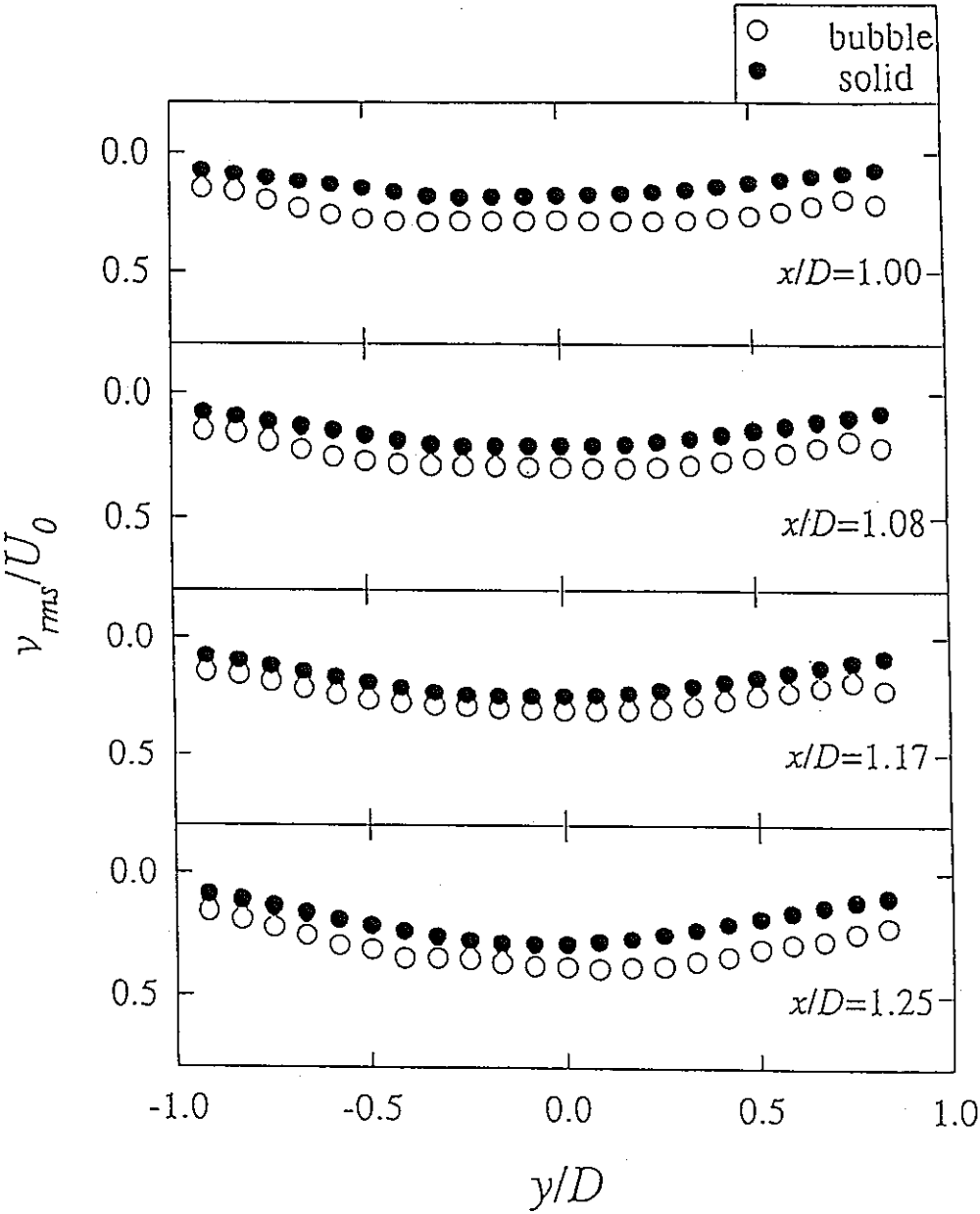
Figure 11 b. Streamwise variation of cross-stream *rms*-velocity v$_{rms}$ /U$_0$.
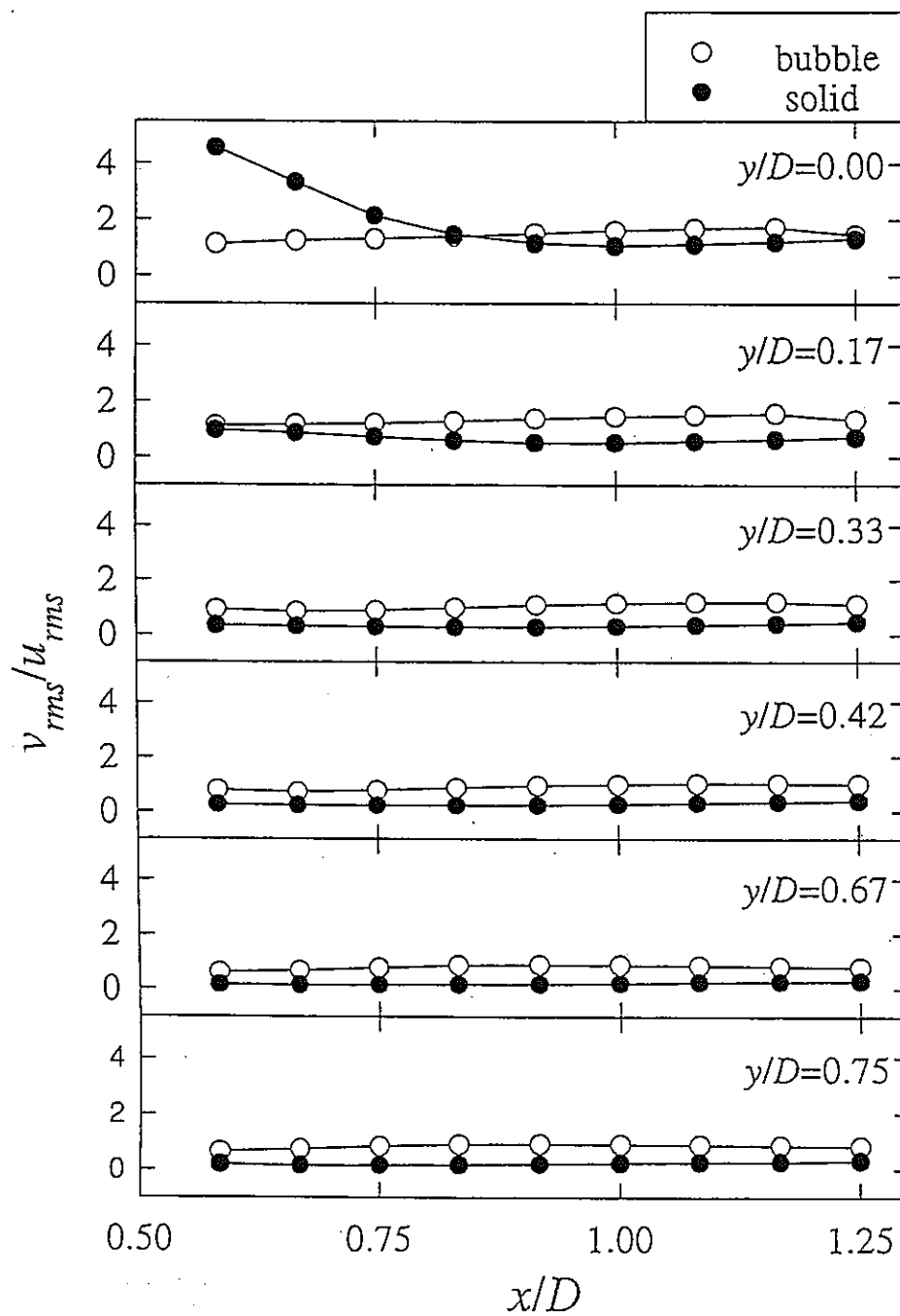
Figure 12. Ratio of cross-streamwise to streamwise *rms* values for solid and bubble.
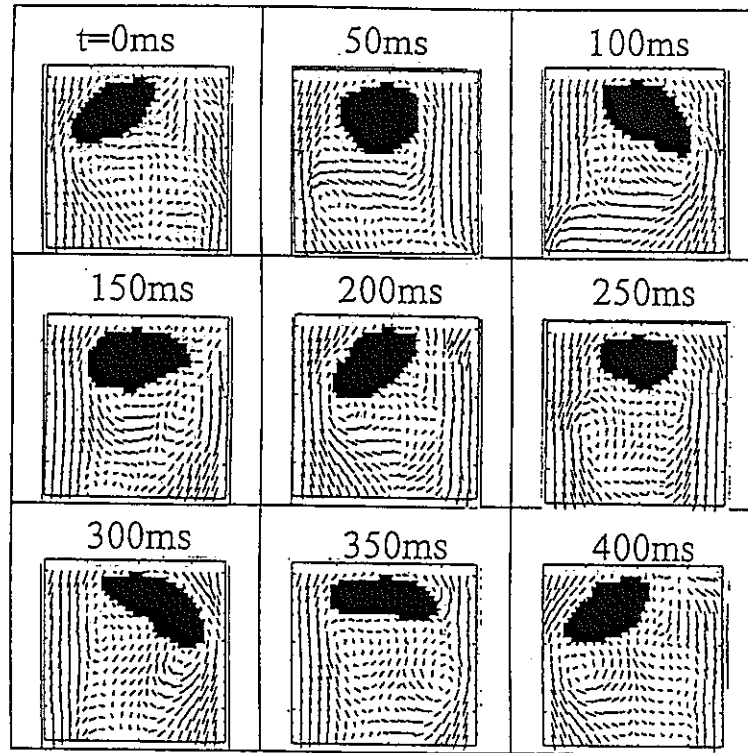
Figure 13. Sequence of shadow-images of the bubble superimposed
on its vector field at 50 ms intervals
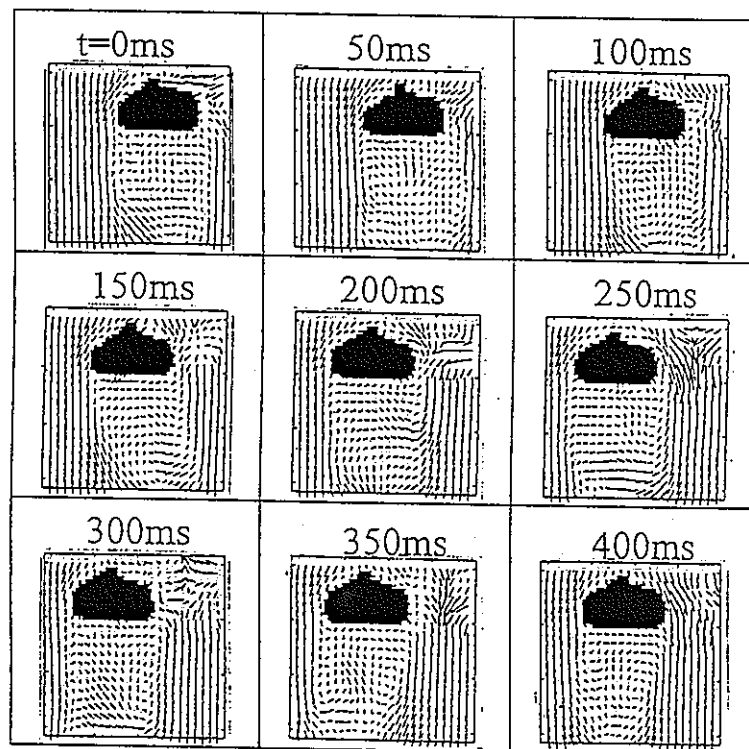
Figure 14. Equivalent sequence at times as indicated for solid.
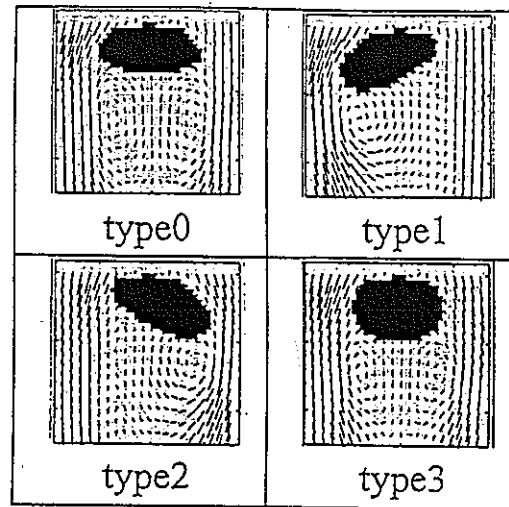
Figure 15. The four selected shapes of the bubble.
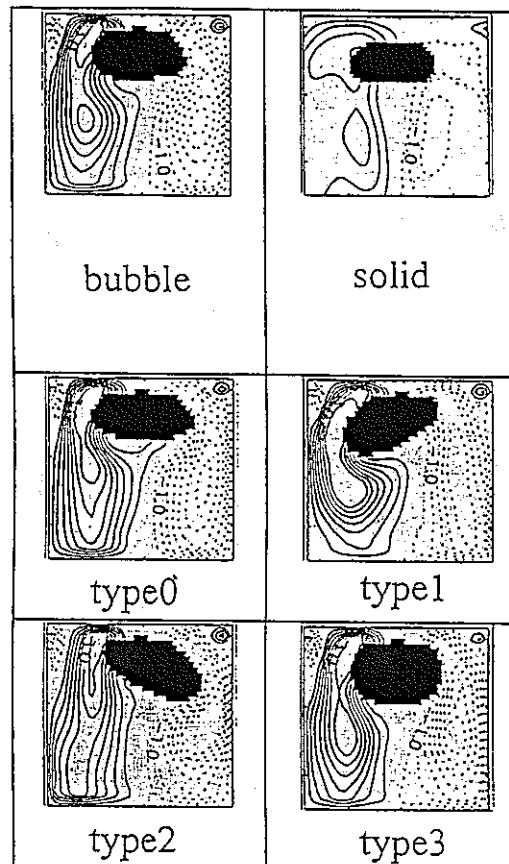
Figure 16. Vorticity contour contrasting the bubble and the solid (upper).
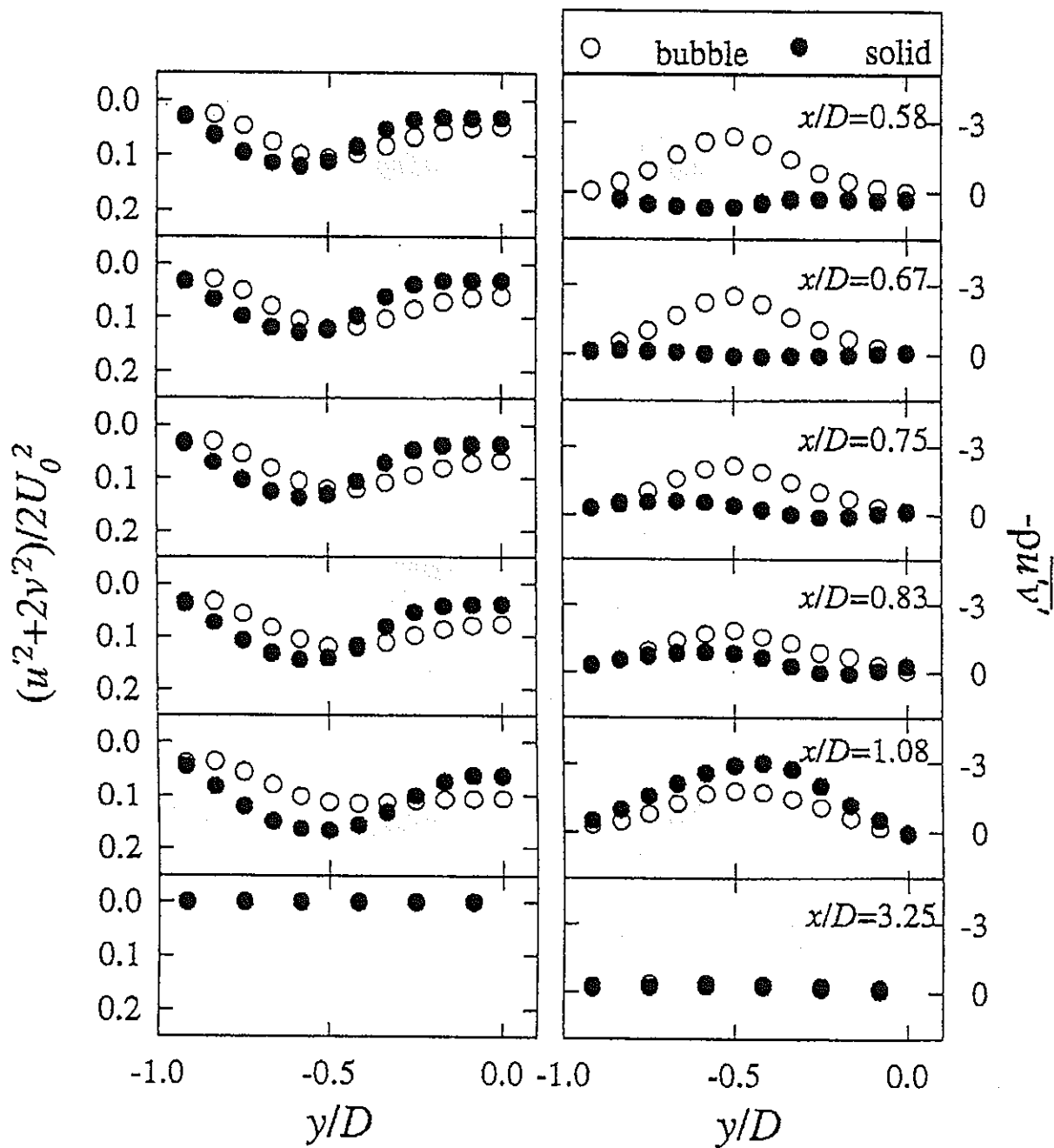Figure 17. Vorticity contours corresponding to the four selected bubble types.
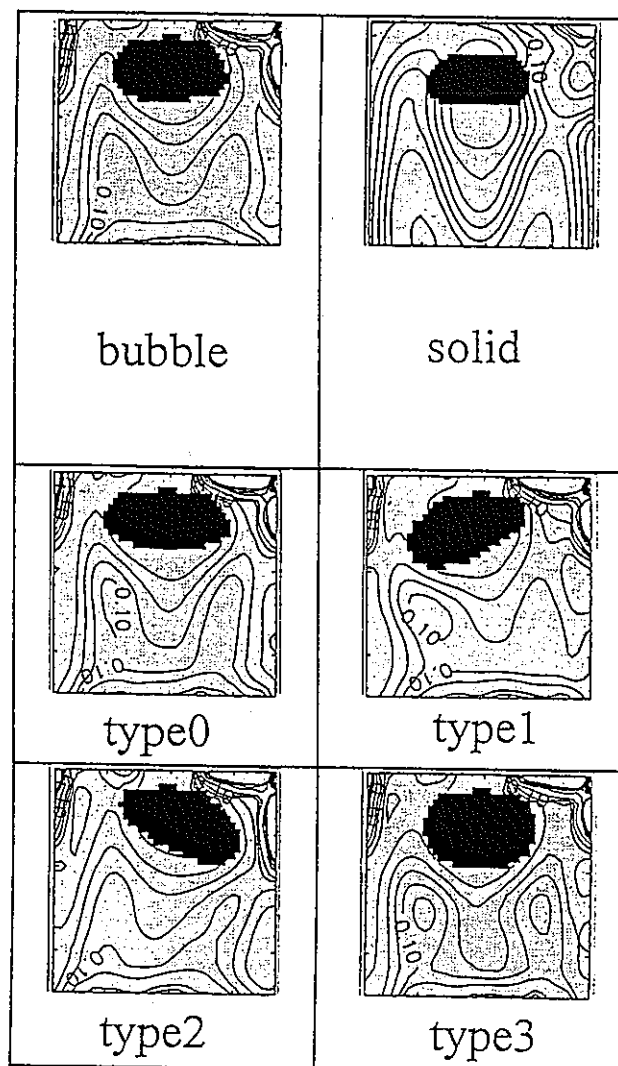
Figure 18. Turbulent kinetic energy contour contrasting the bubble
versus the solid (upper).
Figure 19. Turbulent kinetic energy contours corresponding to
the four selected bubble types.

Figure 20. Turbulent kinetic energy and Reynolds stress distributions for selected streamwise locaitons contrasting the bubble versus the solid.
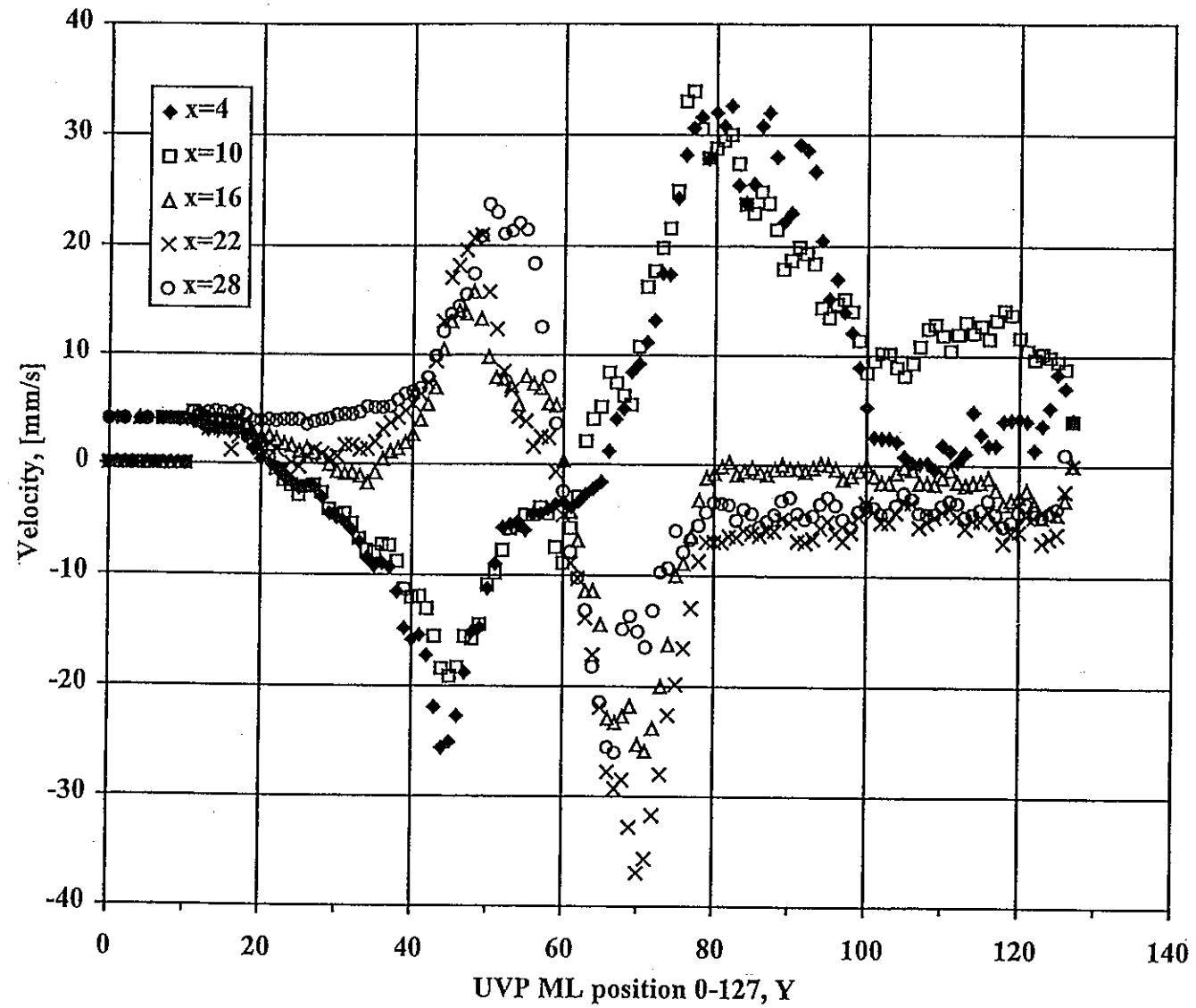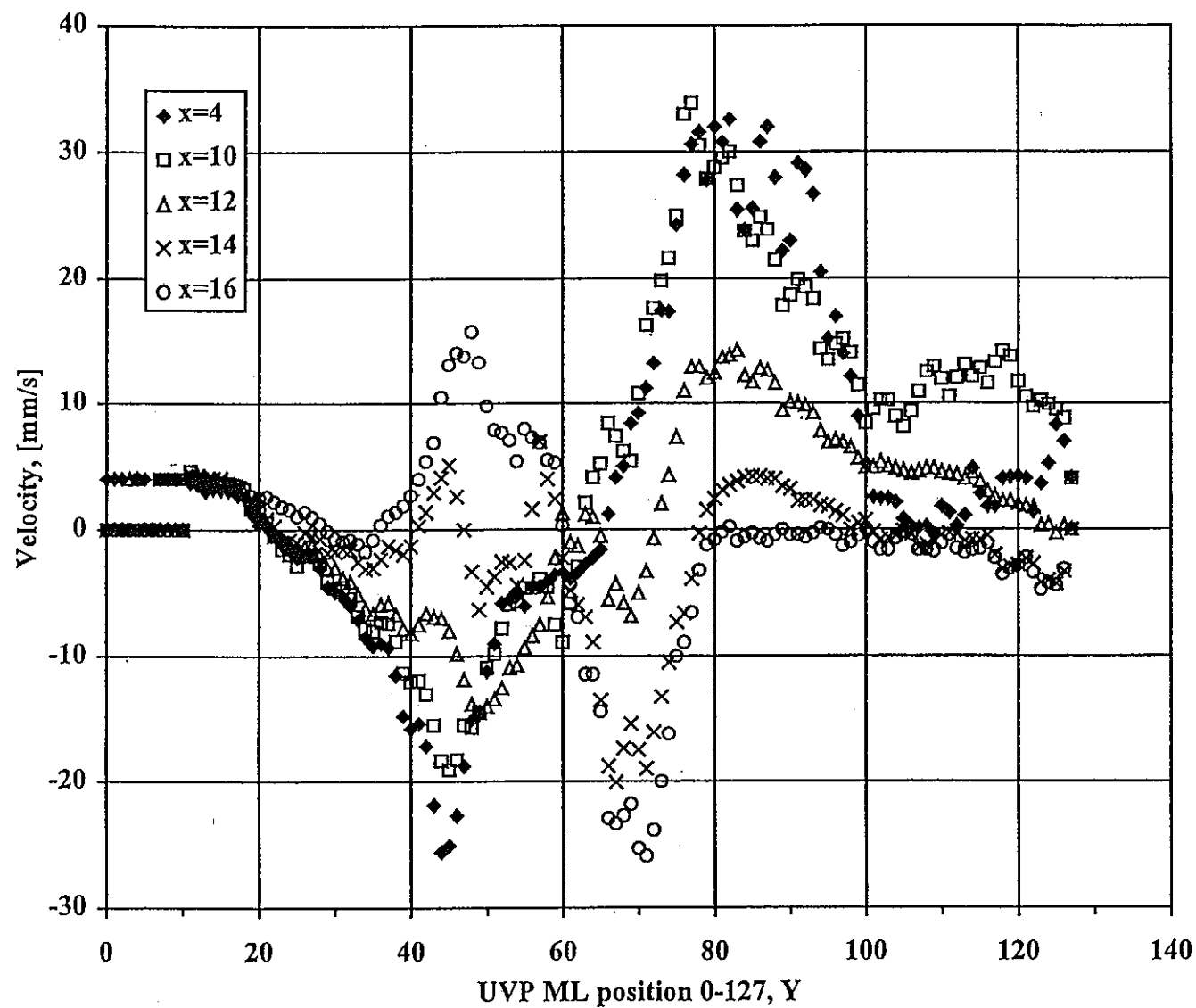
Figure 21. Average velocity for selected distances downstream from a single-bubble.

fn: d:/keio2xav.xls

Figure 22. Average velocity for distances downstream from a single-bubble. Transition from near- to far-wake.
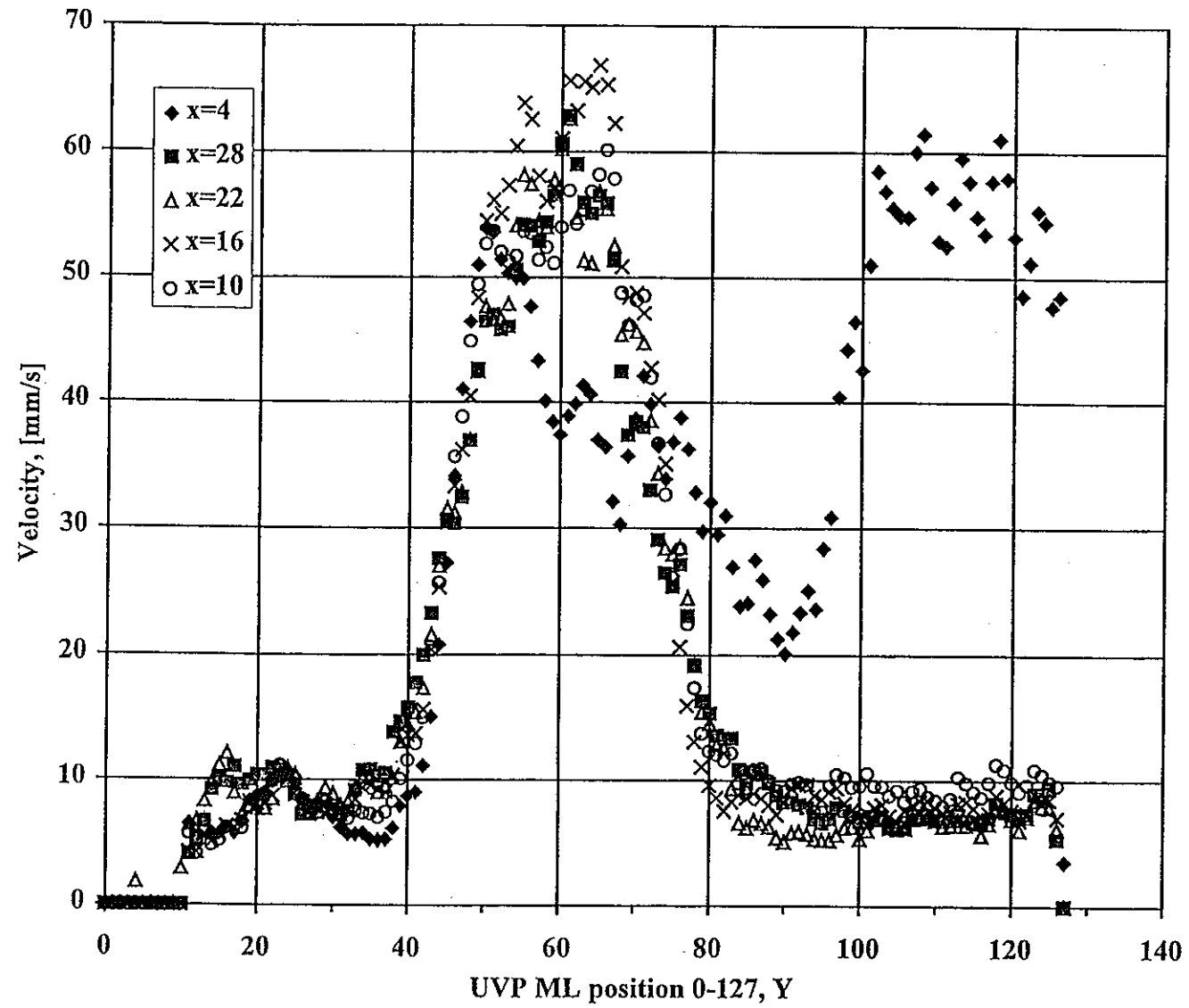
Figure 23. Standard deviation of velocity for selected distances downstream from a single-bubble.
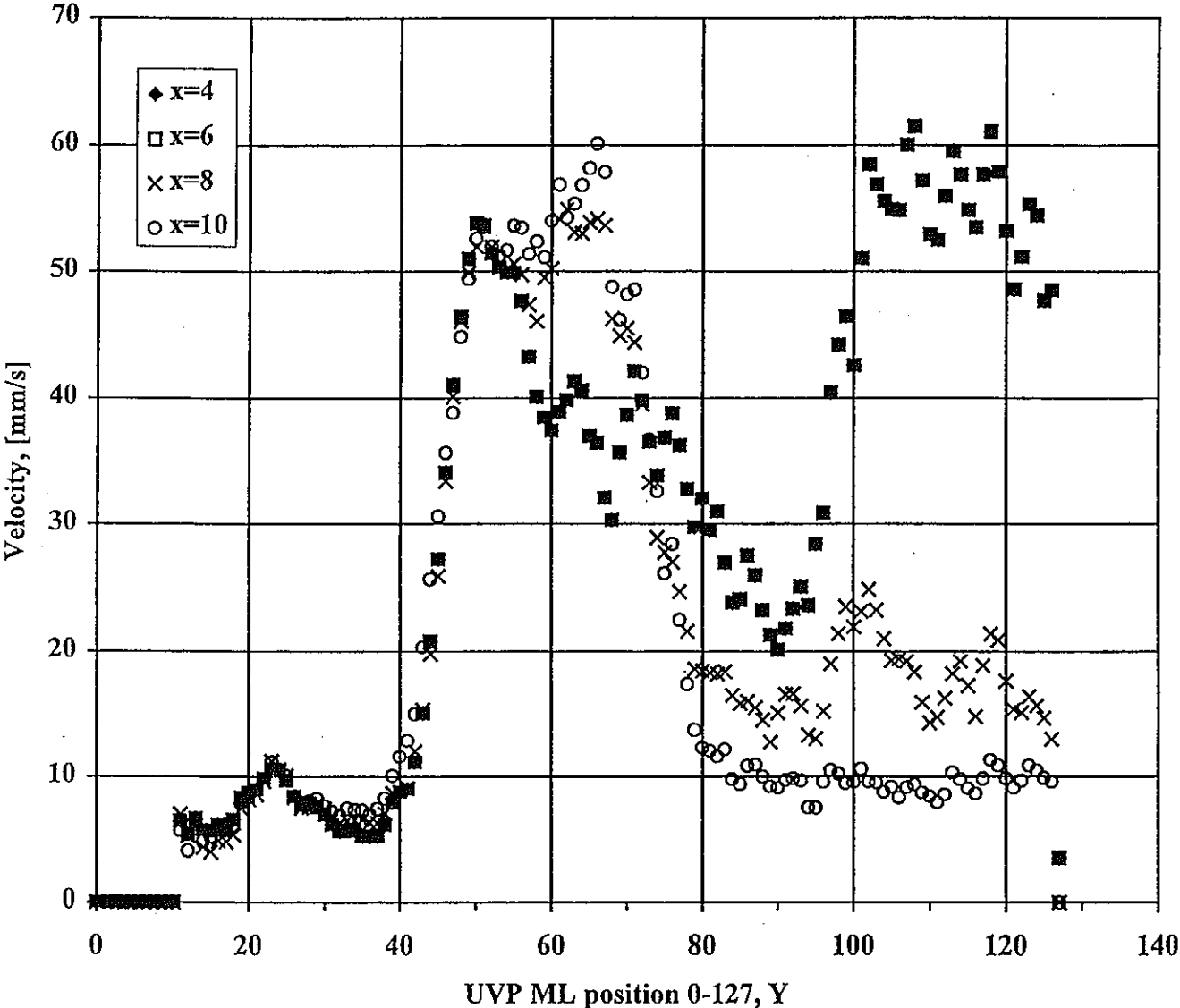
fn:d:keio2xsd.xls Figure 24. Standard deviation of velocity for distances downstream from a single-bubble. Transition from near- to far-wake.
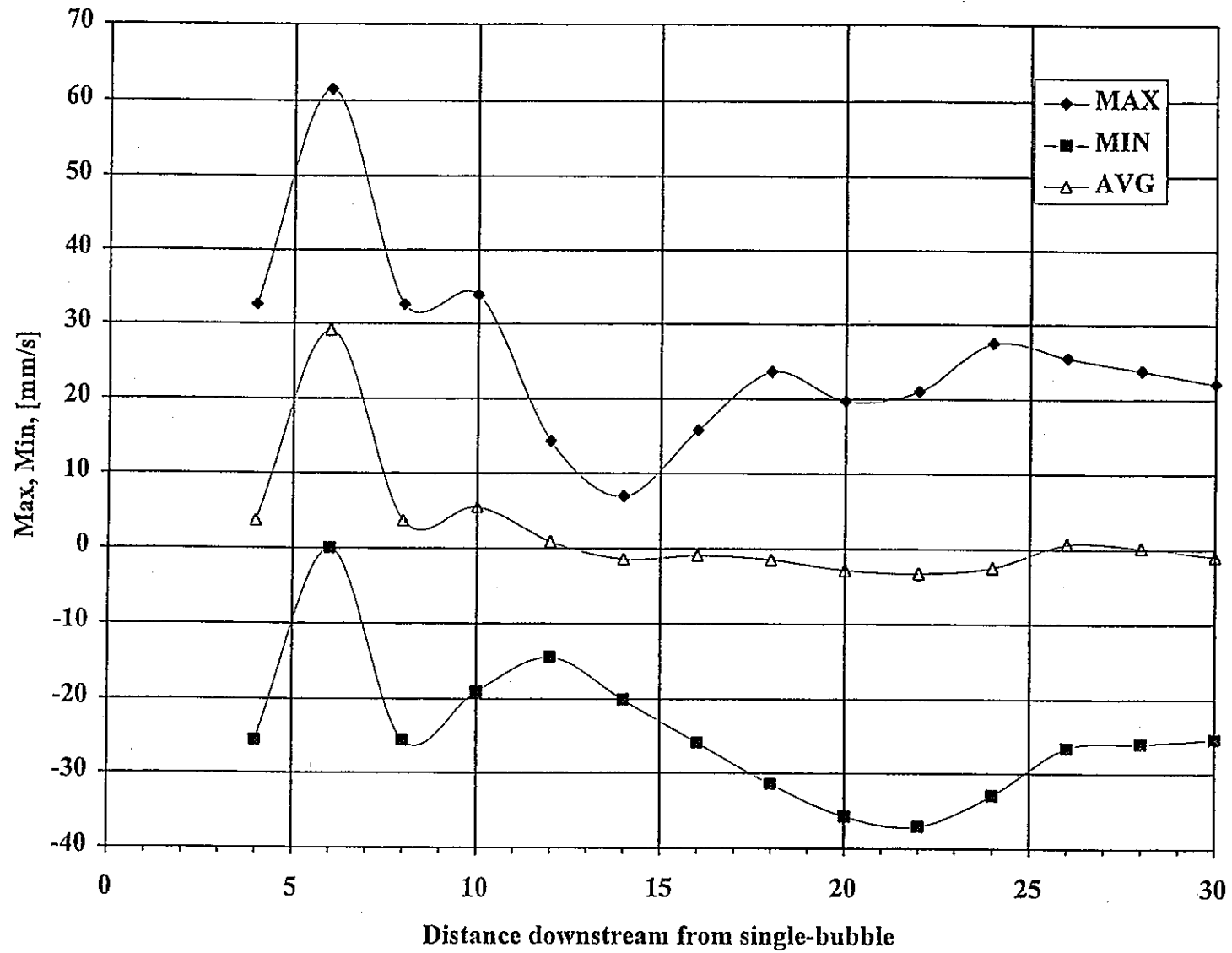
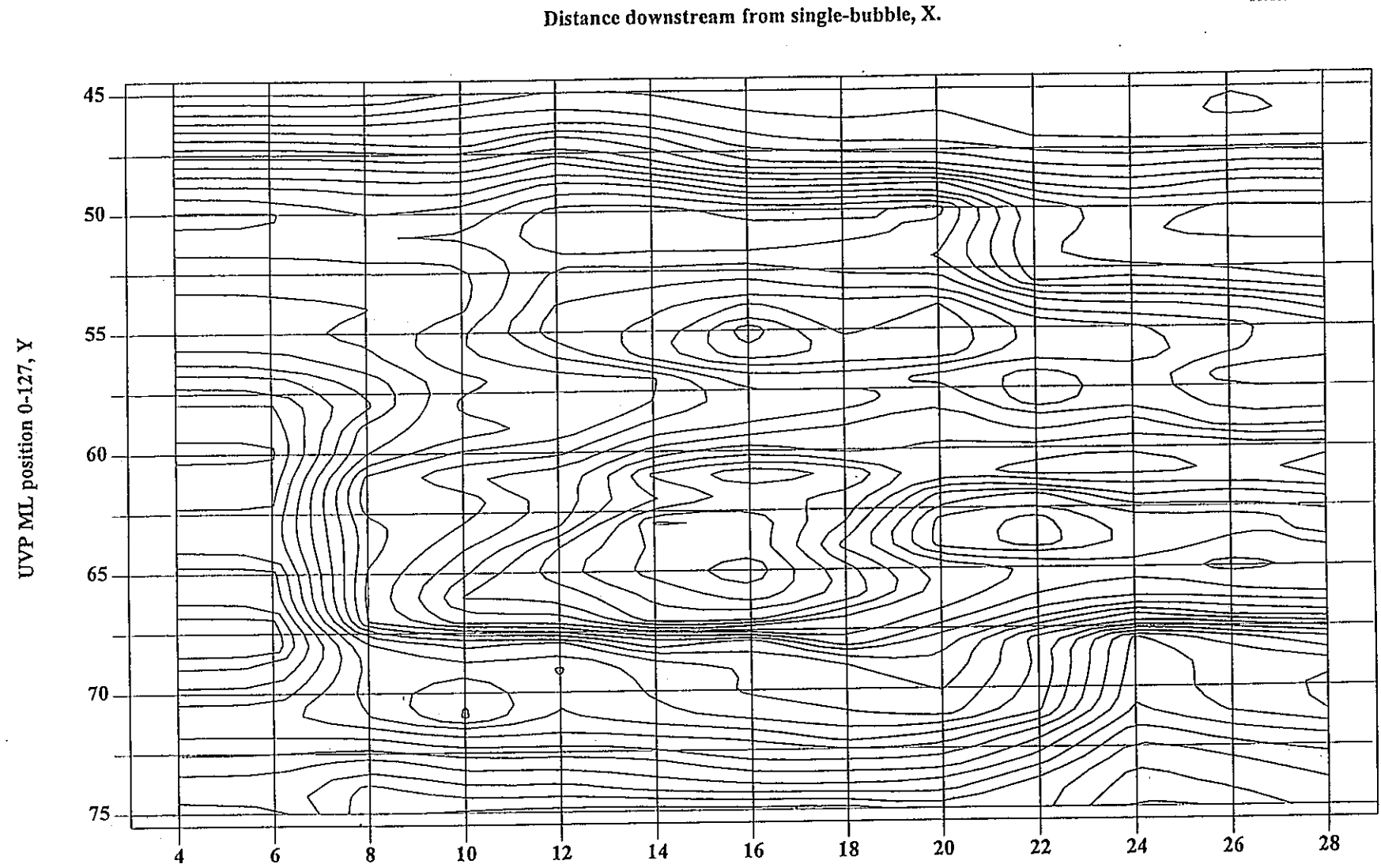Figure 25. Maximum, minimum and average of spanwise (Y) profile for single-bubble.

Distance downstream from single-bubble, X.

Figure 26. Estimated turbulent kinetic energy distribution.

Appendix A:

Image capturing timing and
calculation algorithm for cross-correlation using the DSP

The Digital Signal Processor chip is one of the most important components of current PIV systems. If the user is using a correlational technique in order to identify particles from image-to-image, one can use the DSP to carry-out many of the repetitve calculations. For example, the Texas Instruments TMS320C30 32 bit floating point DSP can carry-out 16 million floating type multiplications and summations per second. Figure A-2 shows the architecture of this DSP and its interface to a PC. Note that due to the availability of several 1K RAM units (to hold data) the DSP can easily handle multiplication and addition simultaneously by using its parallel multiplier and arithmetic logic unit (ALU).

A 2D cross-correlation R(a, b) is defined as follows,

$$R(a, b) = \{\Sigma_0^{n-1}\Sigma_0^{m-1} (f_{(i,j)} - f_{av})(g_{(i,j)} - g_{av})\} / \{\sqrt{\Sigma_0^{n-1}\Sigma_0^{m-1}} (f_{(i,j)} - f_{av})^2\}\{\sqrt{\Sigma_0^{n-1}\Sigma_0^{m-1}} (g_{(i+a,j+b)} - g_{av})^2\}$$

where $f_{av} = (\Sigma_0^{n-1}\Sigma_0^{m-1}f_{(i,j)}) / n \times m$, $g_{av} = (\Sigma_0^{n-1}\Sigma_0^{m-1}g_{i,j}) / n \times m$

and f, g are the pixel values of the reference and corresponding matrices, a, b are the displacements from the reference matric and n, m are the pixel numbers for the x,y direction of t. Substituting f and g into the correlation equation yields,

$$R(a, b) = \{nxm\Sigma_0^{n-1}\Sigma_0^{m-1}(f_{(i,j)} \times g_{(i+a, j+b)})\} / \{\sqrt{(nxm\Sigma_0^{n-1}\Sigma_0^{m-1}(f_{(i,j)}^2 - (\Sigma_0^{n-1}\Sigma_0^{m-1}f_{(i,j)})^2)}\}\{\sqrt{(nxm\Sigma_0^{n-1}\Sigma_0^{m-1}(g_{(i,j)}^2 - (\Sigma_0^{n-1}\Sigma_0^{m-1}g_{(i,j)})^2)}\}$$

Here the summation of f and f^2 only have be calculated once at the beginning of the calculation procedure. The summations of g, g^2 and f x g must however, be calculated for each a,b. The DSP is adept at multiplying and accumulating the partial sums so that to begin the reference and corresponding images are stored sequentially on the "on-chip" RAM0 and RAM1 (see Fig. A-3) and the summation of the product, f xg, is calculated. At a=b=0 the meshed part of G is stored to RAM1 where f x g is calculated. At b=1 a new part of G (see horizontal strip) is stored at the top of RAM1 whereupon the summation of f x g is calculated, after setting the index-pointer to the top of the next region. The index-pointer provides the location for multiplying in RAM1. This index-pointer is incremented after the calculation of f x g until the summation is finished. At the bottom of RAM1, the index-pointer is automaticaly reset to the top of RAM1. This is called "circular addressing" and is prepared as a initial routine of the DSP. So until b=m-1 this process is repeated. At a=1 the same sequence is conducted.

As for the summation of g, the initial step is to store the summation of each row of width m (in G) into BUF1 sequentially (see Fig. A-4). At b=0, the summation of g is obtained from the n successive values in BUF1 into ACC. At b=1, the first value of BUF1 is subtracted from ACC and the $(n + 1)$th value is added so that ACC assumes

the summation of g at b=1. This algorithm is then repeated for the summation of g and for the summation of g^2 (see Fig. A-5).

Finally it was found that data transfer from the CPU to RAM0 and RAM1 was efficient when done in parallel sequence as schematically shown in Fig. A-6.
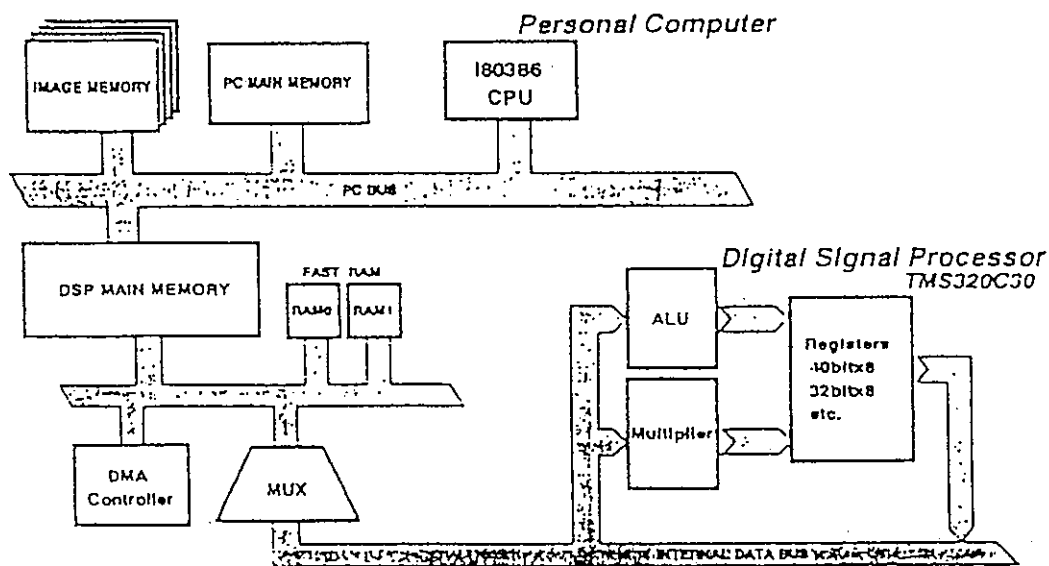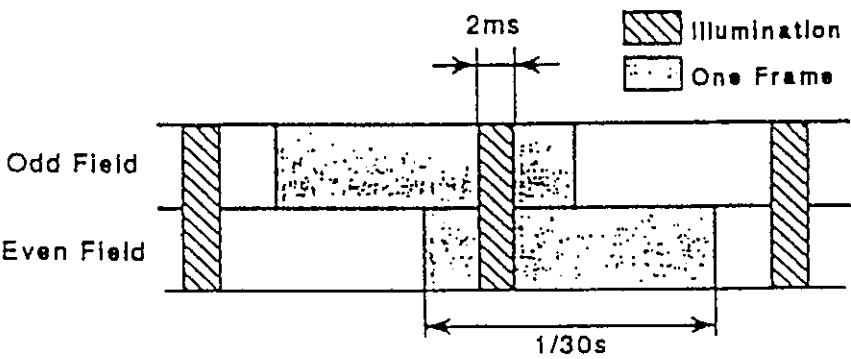
Figure A-1. Schematic of odd-even CCD interlaced mode with timing
of laser pulses (top).
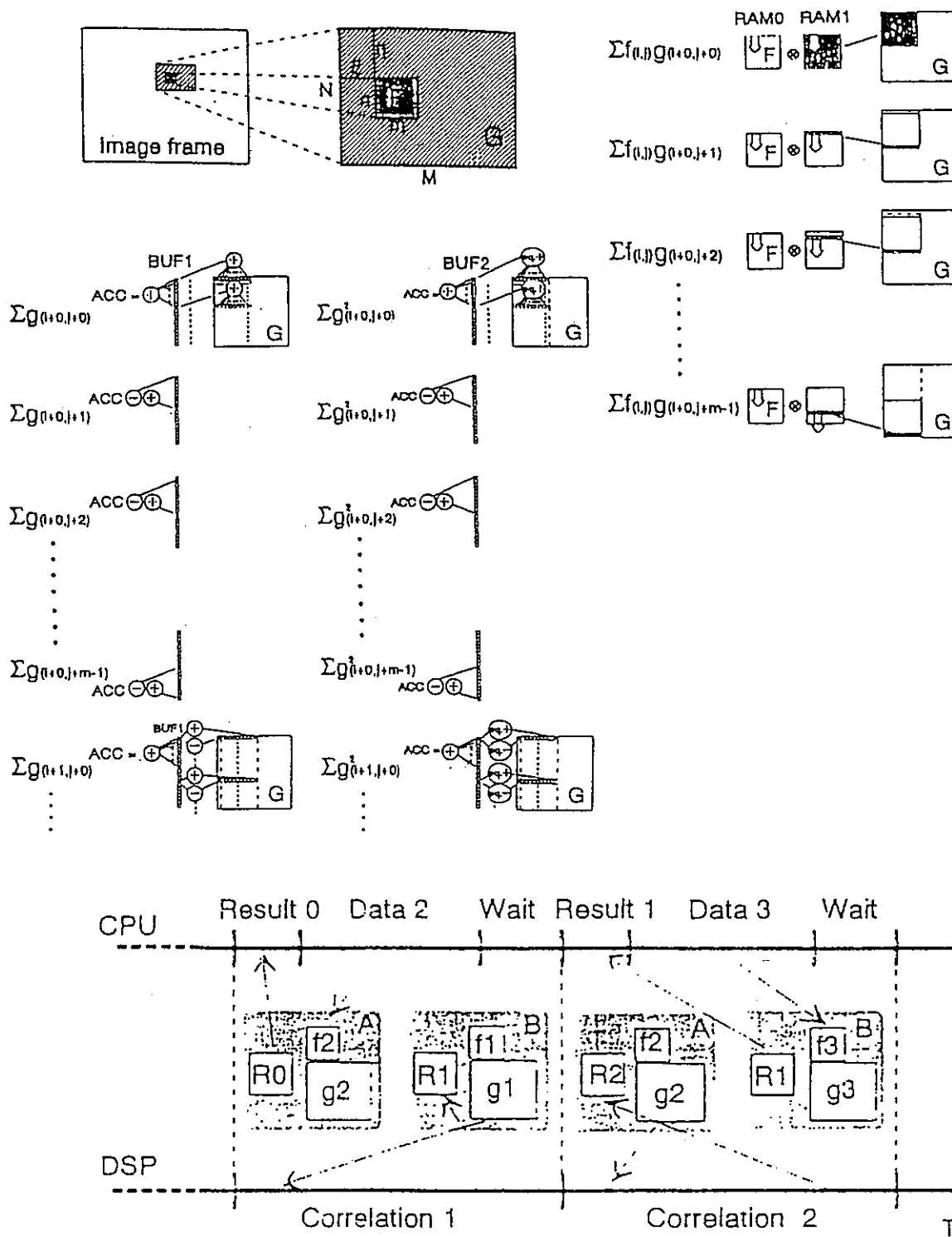Figure A-2. Architecture of DSP and interface to PC.

Figure A-3. Calculation logic for summation of f x g with
reference image frame (top).
Figure A-4. Calculation logic for summation of g and g² (middle).
Figure A-5. Timing and data assignment logic between DSP and CPU (bottom).

Appendix B

Laser Induced Fluorescence (LIF) and Rhodamine B

The fluorescence phenomenon (discovered independently of PIV) which is used describes a light-induced chemical fluorescence that is dependent on both concentration and temperature. The fluorescence intensity (I) can be described by

$$I = I_o A \; \Phi \; \varepsilon L C$$

where I_o is the intensity of the excitation beam, C is the concentration of fluorescence, ε the molar absorptivity, Φ the quantum yield, A the fraction of the available light collected and L the sampling length along the incident beam. In the case where the concentration and absorptivity are constant, the fluorescence intensity is known to have a negative correlation with temperature; that is, as the temperature increases the fluorescence intensity (*FI*) decreases. However, the specific relationship between *FI* and temperature must be generated from a calibration experiment for the specific fluorescent dye to be used. In our applications we used Rhodamine B dye which absorbs green light and emits orange light as shown in Appendix B, Fig. 1. Its intensity varies 2% / degK at 300K. It is also known that Rhodamine B exponentially loses its intensity with time after time and when prepared as an aqueous solution it is sensitive to oxygen molecules and/or metal ions which act as "contaminants" with respect to fluorescence.

In Appendix B, Fig. 2 we show the calibration curve for Rhodamine B plotting the normalized intensity versus the temperature.The calibration can be carried out as follows. Typically a (Ar-Ion) laser beam expanded by a cylindrical lens excites the Rh-B solution contained in a glass dish sitting on a Peltier device which varies the temperature. A CCD camera detects the fluorescence intensity of the Rh-B solution and the images are stored in a computer, typically via a frame grabber board. The temperature of the solution is measured with a thermocouple while a photo-detector monitors and corrects any fluctuation in the laser power. The intensity is recorded over the temperature range of interest for several concentrations of the Rh-B dye and excitation beam intensities. The calibration curve shown in Fig. 2 was normalized by the intensity at 303K and second-order least-square correlated. Thus $I_c = aT^2 + bT + c$.

If the ratio of the measured intensity I to a reference intensity I_{ref} at the reference temperature T_{ref} is calculated along with the inverse function of the calibration curve T_c versus I_c one can deduce the temperature field as,

$$T(x,y) = T_c [\; T_c(T_{ref}) \; (I(x,y)/I_{ref}(x,y))]$$

As for the local pixel value of intensity of a digitized image, an average intensity from several pixels was used in our applications. A non-linear disparity between the input and output of a CCD camera (especially at low light intensities) also has to be compensated for by implementing a calibration curve for the non-linearity.
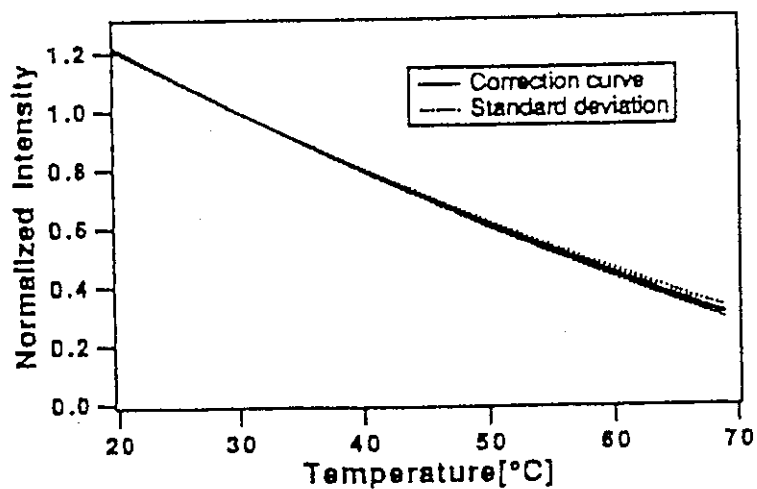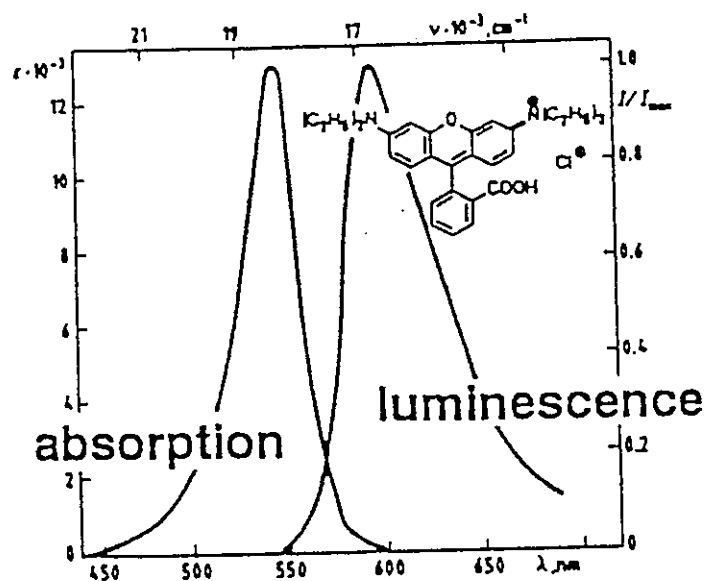
Figure B-1. Absorption and luminescence spectra of rhodamine-B (top).
Figure B-2. Relationship between temperature and luminescence intensity.

Appendix C

Ultrasound Doppler velocimetry principles and

UVP operational parameters.

Ultrasound Doppler velocimetry

- Principle works on ultrasound (acoustical) echography; time-of-flight measures position; Doppler shift enables calculation of velocity; sign of Doppler shift indicates direction of flow.

- Ultrasound transducer is pulsed; ultrasound is reflected from tracer-particles;tracer particles are added in to water; in sodium, *impurities* act as tracer-particles.

- Velocity profile is constructed along 128 points; magnitude and sign.

- 1024 profiles are taken during each measurment run.

Spatio-temporal velocity data is recorded.
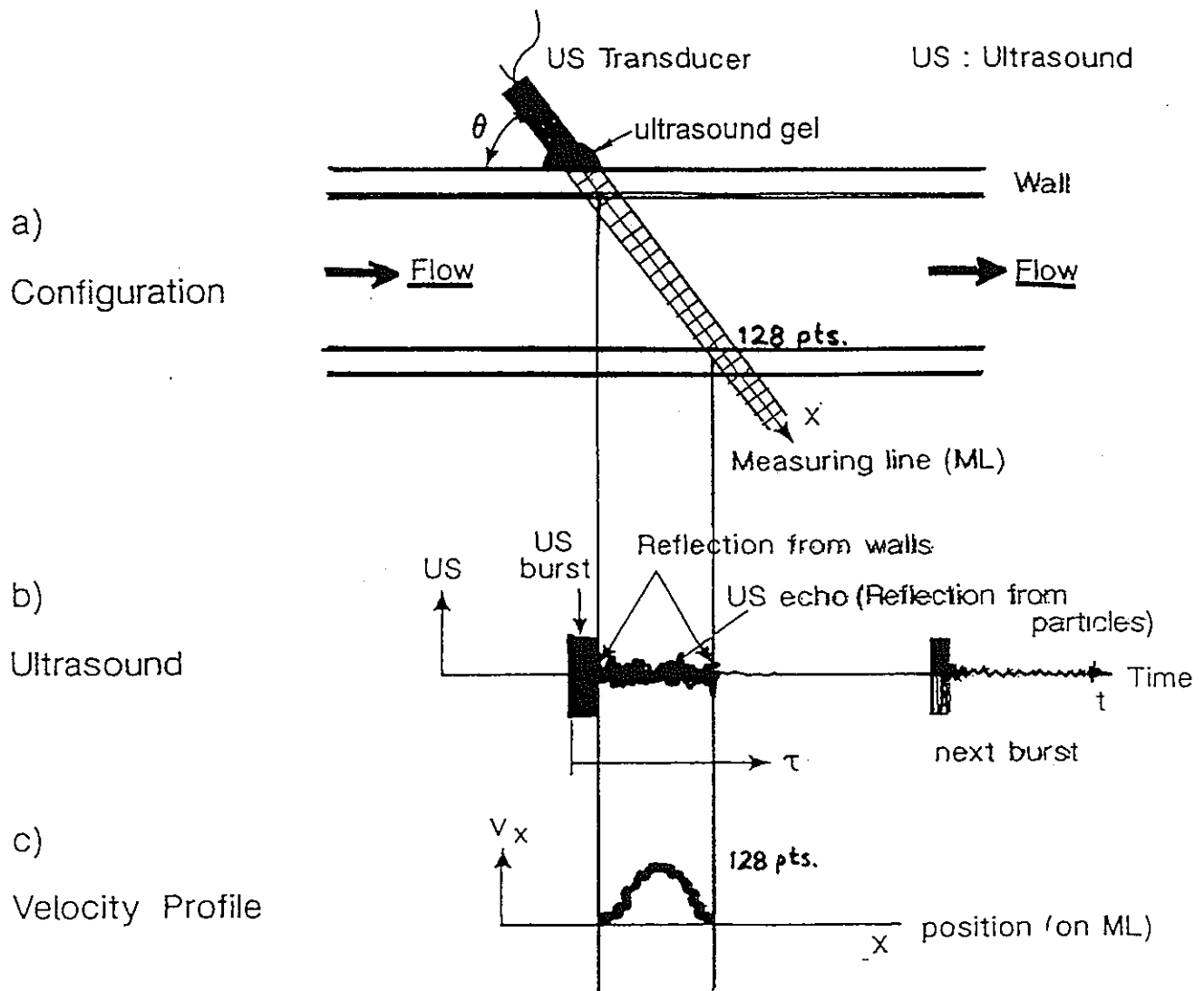
Figure C-1. Principle of ultrasound Doppler velocimetry.

Table C-1.Typical UVP operational parameters used in this work

US Basic Freq.:	4 (M H z)
Channel Distance:	0 . 7 (m m)
Starting channel:	1 1 (m m)
Ending channel:	1 0 6 (m m)
F p r f:	2 1 5 7 (H z)
Sound Velocity:	1 4 8 0 (m / s)
Storing Interval:	0
Trigger mode:	M a n . 1 0 2 4
Screen Type:	N o r m a l
Emission Voltage:	1 5 0 V
R F Gain start:	9
R F Gain end:	9
N o . B l o c k s:	1
N o . P r o f i l e s / B l k:	1 0 2 4

Table C-2. A comparison of LDA and UVP
for a typical flow measurement application.
[Cf: Application Software Package #3, UVP Flow Mapping System, FlowBiz Tokyo, Vers. 1.0, Jan. 1996]

A flow mapping system
using the UVP Model X2/3-PS

1 Introduction

One of the advantages of UVP method is that it offers a very efficient way of flow mapping. This is due to its line-measurement of velocity distribution in a fluid flow. Comparison with a conventional point-measurement method for flow mapping , LDA as an example, is given in the table below. It shows that the UVP is about 100 times more efficient.

LDA		UVP
1 color 20x20x128 10 sec/point 142 hours	1 Component Probe/system Scan. Grid Meas. Time Total time	1 TDX 20x20(x128) 35 sec/line 4 hours
3 colors 20x20x128 10 sec/point 142 hours	Vectoral (3D) Probe/system Scan. Grid Meas. Time Total Time	Array TDX 3x20x20(x128) 35 sec/line 12 hours
2.5 hours	Oscillating pipe flow	2.5 minutes

Table 1 Comparison of the flow mapping system
for LDA and UVP system

The UVP Model -PS is designed to use multiple transducers for flow mapping. In order to realise the efficient flow mapping system, it is more convenient to use multiple transducers which are arranged such that required flow area is entirely covered than moving a single transducer from one place to another

This brochure gives a guideline how to build such a flow mapping system using the UVP Model -PS. All these components which consist of the system can be found in the market. Some equipments are recommended in the market.